REVIEW

Check for updates

Defects in complex oxide thin films for electronics and energy applications: challenges and opportunities

Weiwei Li, [iD] *[a] Jueli Shi,[b] Kelvin H. L. Zhang [iD] *[b] and Judith L. MacManus-Driscoll*[a]

Complex transition-metal oxides (TMOs) are critical materials for cutting-edge electronics and energy-related technologies, on the basis of their intriguing properties including ferroelectricity, magnetism, superconductivity, (photo- and electro-) catalytic activity, ionic conductivity, *etc.* These properties are fundamentally determined by the partially occupied TM d orbitals and the corresponding local coordination environments, which are sensitive to defects (or impurities), compositions, grain boundaries, surface and interfaces, *etc.* Recently, motivated by the advance in thin film epitaxy techniques, the complex oxide research community has shown great interest in controlling defects for enhanced or even unprecedented functional properties. In this review, we provide an overview on recent progress in tuning the functional properties of TMO thin films *via* defect engineering. We begin with a brief introduction to the defect chemistry of TMOs, including types of defects and their effects on local atomic structure, electron configurations and electronic structure, *etc.* We then review recent research efforts in engineering defects in TMOs for novel functionalities, such as ferroelectricity, magnetism, multi-ferroelectricity and dielectricity, two-dimensional electron/hole gas, metal–insulator transitions, resistive switching, ionic conductivity, photo-electrocatalysis, *etc.* We also provide insights into understanding the defect-structure–property relationship from the perspective of electronic structure. Finally, challenges and perspectives on control of defects for design of novel devices are discussed.

[a] *Department of Materials Science and Metallurgy, University of Cambridge, 27 Charles Babbage Road, Cambridge, CB3 0FS, UK. E-mail: wl337@cam.ac.uk, jld35@cam.ac.uk*
[b] *State Key Laboratory of Physical Chemistry of Solid Surfaces, College of Chemistry and Chemical Engineering, Xiamen University, Xiamen 361005, China. E-mail: kelvinzhang@xmu.edu.cn*

1. Background for complex transition-metal oxides

Complex transition-metal oxides (TMOs) have attracted intensive research interests in both materials science and condensed matter physics over the past decades, largely due to their broad range of properties from insulating to semiconducting or
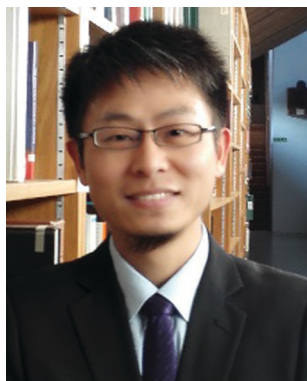
Weiwei Li received his PhD degree from Soochow University in 2015. Currently, he is a research associate in the Department of Materials Science & Metallurgy at the University of Cambridge. His research interests focus on the complex functional oxide thin films for (opto-)electronic devices and energy conversion/storage.

Weiwei Li

Jueli Shi received his bachelor degree in energy chemistry from Xiamen University in 2018. He is currently a PhD candidate at college of Chemistry and Chemical Engineering, Xiamen University under the supervision of Prof. Kelvin H. L. Zhang. His research interest focusses on the synthesis and properties of oxide semiconductor thin films.

Jueli Shi

metallic, exhibiting many fascinating phenomena including (anti-)ferromagnetism (FM), (anti-)ferroelectricity (FE), multi-ferroelectricity, ionic conduction, colossal magnetoresistance (CMR) and high temperature superconductivity, *etc.* These exotic properties arise from a complex hierarchy of competing interactions among spin, charge, orbital and lattice degrees of freedom, which are fundamentally underpinned by the electronic states of the partially occupied TM d orbitals. Driven by recent advances in fabrication of high-quality epitaxial thin films with an atomic-scale control *via* pulsed laser deposition (PLD) and molecular-beam epitaxy (MBE), TMOs are receiving fast-growing interests and hold great potential to outperform conventional semiconductors. However, the epitaxial thin films required for most applications are imperfect with far from optimum performance. Hence, many promised applications spanning beyond-Si information and communications technology (ICT) devices to a vast range of energy-related devices and sensors currently remain just promises. Furthermore, TMOs are also promising candidates as (photo-)electrocatalysts for the production of "green fuels" (principally H_2, syngas and even liquid hydrocarbons) by splitting H_2O and reducing CO_2 and as electrocatalysts and ionic conductors in solid oxide fuel cells (SOFCs) for the combustion of "green fuels" (*e.g.*, H_2) to generate electricity with high efficiency. The production and use of "green fuels" are widely seen as a promising pathway towards a global sustainable energy future.

In the field of microelectronics, the properties of IV elemental semiconductors (*e.g.*, Si), III–V compound semiconductors (*e.g.*, GaAs), II–VI compound semiconductors (*e.g.*, ZnO) and their implementation in devices such as transistors, photodetectors, light-emitting diodes, and solar cells depend on the control and distribution of defects, dopants, surface and interface electronic states, with spatial scale often on the sub-part-per-million level. Recently, with the simultaneous advances in thin film synthesis, characterization, and modelling of TMOs, engineering the defects and interface in TMOs have been widely explored as a route to enhance and even create novel functionalities in TMOs for new devices.[1] Although significant progresses have been made in the

past decade (will be discussed later), a deep understanding of the defect chemistry in complex TMOs still lag behind that in conventional semiconductors. This is because: (1) TMOs have many constituent elements and can accommodate a wide variety of defects, including oxygen vacancies (V_O), cation vacancies (V_C), interstitial defects, local structural distortions, grain boundaries, domain walls, misfit dislocations, and impurities such as $H^{+/-}$, Li^+, *etc.* (2) Due to the ionic nature of TMOs, the transition energy of defects in TMOs are usually high and the extra charges left by defects are usually localized, therefore defects in TMOs usually cannot lead to a significant change in the electrical conductivity as present in conventional semiconductors. (3) Although theoretical modeling has also been widely used to study the thermodynamics and electronic states of defects, the fundamental issue of *ab initio* density functional theory (DFT) in dealing with the many-electron system gives rise to a considerable underestimation of the bandgap of TMOs, and therefore leads to many inaccuracies in predicting the properties of defects.[2–4]

In this review, we will provide an overview on recent progress in tuning the functional properties of complex TMO thin films *via* defect engineering. We will begin with a brief introduction on the types of defects and their consequences on electronic structures. We will then provide a detailed review on how these defects can change functional properties (*e.g.*, ferroelectricity, magnetism, multi-ferroelectricity, dielectricity, optical and transport properties, ionic conduction, and photo-electrocatalytic activity) and how these properties can be experimentally analyzed and evaluated. Finally, challenges and perspectives of tailoring TMOs properties through defect engineering are discussed.

2. Defect chemistry in complex transition-metal oxides

2.1 Types of defects

Since this review focuses mainly on TMOs with a perovskite structure, we will use perovskite oxides as examples to illustrate the types of defects present in TMOs. Perovskite TMOs have a

Prof. Kelvin H. L. Zhang is a professor at college of Chemistry and Chemical Engineering, Xiamen University. His current research interests focus on the synthesis and properties of complex metal oxide thin films and heterostructures relevant to application in oxide electronics and electrocatalysts. He obtained his PhD degree in chemistry Oxford University of in 2012, followed by working as a postdoc at Pacific Northwest

Kelvin H. L. Zhang

National Laboratory and as a Herchel Smith Fellow at University of Cambridge from 2015 to 2017.

Prof. Judith MacManus-Driscoll is Professor in the Materials Science & Metallurgy at the University of Cambridge. She is also Royal Academy of Engineering Chair in Emerging Technologies. Her research work is in the area of oxide thin film engineering for low power electronic and energy devices. She is interested both in understanding basic functionalities and in engineering new interfacial-driven properties.

Judith L. MacManus-Driscoll

Fig. 1 The different types of defects in transition metal oxides (TMOs). (a) V_O: missing oxygen atoms from lattice sites; V_C: missing cation atoms from lattice sites; anti-site disorder: swapping the cation/oxygen positions; interstitial impurities: ions occupying interstitial crystallographic sites. (b) Misfit dislocation: a missing or dangling bond in the lattice between two TMO layers with different lattice parameters. (c) Grain boundary: the interface between two grains with different crystalline orientations. (d) Polar discontinuity: the interface between nonpolar and polar TMOs. (e) Domain wall: the boundary between two neighbouring domains. (f) Ionic doping: the process of moving ions into or out of TMOs by an external stimuli. (g) BO_6 octahedral distortion: the tilting of an oxygen octahedron in TMOs.

chemical formula of ABO_3, as sketched in Fig. 1. A-sites are usually alkaline rare-earth cations, while B-site cations are usually TM cations with partially filled d orbitals octahedrally coordinated by six oxygen anions.

Point defects represent a deviation from the long-range periodicity of crystal lattice. The key types of point defects include vacancies (*e.g.*, oxygen vacancies, V_O and cation vacancies, V_C), interstitials and anti-site defects (Fig. 1a). A remarkable example can be found in the perovskite $SrTiO_3$, where the introduction of V_O can turn the insulating $SrTiO_3$ into a metallic state, and even a dome-shaped superconducting phase dependent on carrier density concentrations.[5–7] Further, the formation of Ti^{3+} ($3d^1$) induced by V_O can lead to a ferromagnetic interaction in diamagnetic $SrTiO_3$.[8] Through the formation of Sr vacancies, room-temperature ferroelectricity can be created in paraelectric $SrTiO_3$.[9] Moreover, by swapping the cation positions between Sr^{2+} and Ti^{4+} to form anti-site cationic defects of Sr_{Ti} or Ti_{Sr}, paraelectric $SrTiO_3$ become ferroelectric at room temperature and highly conductive channels can also be formed and controlled by the ferroelectric polarization.[10]

Owing to the discontinuity of lattice and chemical environment, the interface provides a more favorable environment for defects with lower formation energy. These interface-related defects contain misfit dislocations (Fig. 1b), grain boundaries (Fig. 1c), polar discontinuity (Fig. 1d), and domain walls (Fig. 1e). Crystalline TMOs usually contain dislocations, grain boundaries, and domain walls, which reportedly exhibit a very different nature from the rest of the bulk matrix. The presence

of these defects can significantly influence properties such as ionic and electrical conductivities, magnetism, and ferroelectricity. For instance, dislocations have been reported to creating ferromagnetic regions in anti-ferromagnetic NiO,[11] while grain boundaries of ferromagnetic $La_{2/3}Ca_{1/3}MnO_3$ can lead to paramagnetic properties.[12] In $SrTiO_3$, the dislocations and grain boundaries are generally considered to be charged largely due to nonstoichiometry, which may account for the unique electrical and ionic transport properties.[13,14] Also, electronic conductivity has been observed at ferroelectric domain walls in the insulating multiferroic $BiFeO_3$.[15]

Oxygen octahedra (BO_6, Fig. 1g) plays a central role in the physical properties of many ABO_3 compounds. Their rotations lead to the reduction of the B–O–B bond angle, with profound consequences for magnetic and transport properties of various perovskite TMOs. In the rare-earth (R) nickelate $RNiO_3$ series of compounds, the reduction of the Ni–O–Ni bond angle is accompanied by a spectacular first-order metal-to-insulator transition,[16] whereas the magnetic superexchange interaction in manganites depends sensitively on the Mn–O–Mn bond angle and bond length.[17] Besides, reversible changes in the structural and electronic properties of TMOs can be achieved with electric fields by moving ions (*e.g.*, H^+ and Li^+, Fig. 1f) into or out of TMOs.[18–21]

2.2 Electronic structure consequences of defects

Due to the strong interactions between structural and electronic structures, coherently strained TMOs films and heterostructures

have emerged as one of the most effective platforms to engineer novel functionalities. The nature of BO_6 rotations and structural deviations from ideal cubic symmetry to alter key structural features like B–O bond lengths strongly influences TMOs electronic structure through properties such as d orbital occupancy and metal–oxygen orbital overlap. Tuning B–O bond lengths of TMOs by strain can break the degeneracy of e_g orbitals by enhancing the electron occupancy in either in-plane $d_{x^2-y^2}$ orbital under tensile strain or the out-of-plane d_{z^2} orbital under compressive strain (Fig. 2a).

Defects, impurities and interface break the regular periodicity of the crystal lattice, and more importantly introduce extra energy levels into the band gap, therefore leading to the change of electronic structure and physical properties of TMOs. The band structure of TMOs generally contains an empty TM nd derived conduction band (CB) and valence band (VB) with O $2p^6$ hybridized with filled TM nd orbitals (Fig. 2b). The energy separation of the empty TM nd and filled TM nd orbitals is induced by the crystal field splitting and/or the intra-atomic electron–electron repulsion energies (U_n). The formation of defects in TMOs will introduce extra electronic states in the bands, leading to a range of novel physical properties.[22–25] The most critical factors of the defects include: (i) the energy positions of extra defect states relative to CB/VB; (ii) the local environment of the defects (coordination numbers and bonding length/angle); (iii) the number of occupied carriers, as schematic illustrated in Fig. 2c–h.

When extra electrons are introduced into the CB or extra holes into the VB, TMOs will become more conductive and sometimes a metallic state can be induced, as shown in Fig. 2c and d. More commonly seen cases would be defect levels with electrons located just below the CB, or the empty level located just above the VB, acting as shallow donors and shallow acceptors (Fig. 2e and f). Under these circumstances, defect levels could provide free electrons or holes by thermal excitation and increase the conductivity. Moreover, the Fermi level will also be changed. When the empty defect levels are located just below the bottom of CB, or levels with electrons are just above the top of VB, the defects will no longer introduce new carriers into the bands or alter the Fermi level, and in turn act as traps for electrons in CB or holes in VB, as shown in Fig. 2g–h. Sometimes the defect levels are far from the band edges, so that the free carriers cannot be generated under normal thermal excitations, these defects are known as deep states.

The creation of defects in ionic oxides such as MgO is difficult, due to the high formation energies.[26,27] However, many TMOs can tolerate high concentrations of defects under equilibrium conditions. These defects are often associated with deviation from ideal stoichiometry of the parent oxides, due to the relative ease of reducing or oxidizing of the metal ions.[23,28,29] Shallow levels are often induced with the break of perfect stoichiometry and determine the conducting behaviors of the resulted TMOs. The nonstoichiometry of TMOs could be
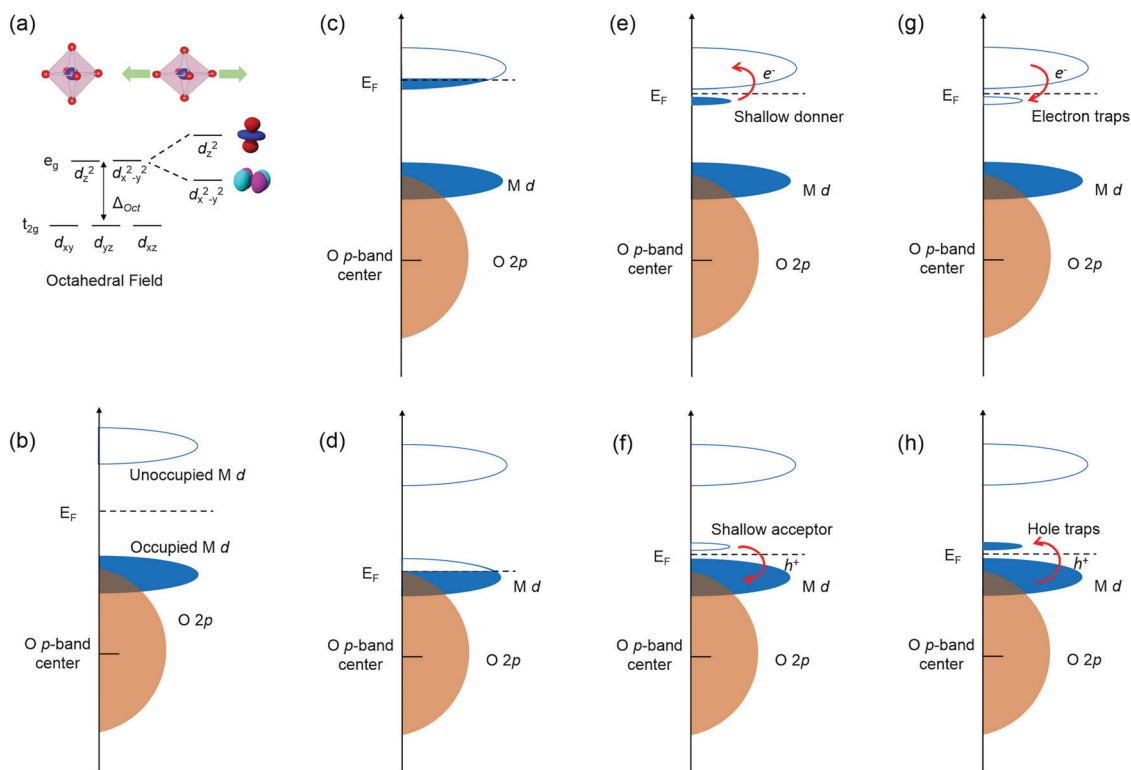
Fig. 2 Electronic Structure of transition metal oxide and the typical defect states within it: (a) d orbital splitting of transition metal oxides through octahedral field. (b) Idealistic band structure. (c) and (d) Extra electrons or holes in conduction band (CB) or valence band (VB). (e) and (f) Defect levels providing free electrons or holes by thermal excitation. (g) and (h) Defect levels acting as traps for electrons and holes.

divided into metal excess and oxygen excess. The metal excess of oxide M_aO_b could be achieved by the introduction of V_O with a formula of $M_aO_{b-\delta}$, or through the introduction of metal cation interstitials with a formula of $M_{a+\delta}O_b$. In both cases, the nonstoichiometry results in the involvement of additional electrons and the related electronic properties depend on the extent of the electrons' binding strength to cationic species. Once sufficient energies are provided to the metal excess oxides, electrons become itinerant and the oxides become n-type conductive. For example, $SrTiO_3$ could form Ti interstitials or V_O to become a n-type semiconductor, or even a metallic state as mentioned in above section.[30–32] Similarly, p-type conductivity could be achieved by extra holes introduced in oxygen-excess phases. These phases can be created by the introduction of metal cation vacancies with a formula of $M_{a-\delta}O_b$, or through the introduction of V_O with a formula of $M_aO_{b+\delta}$.[33–36] The p-type conductivity of undoped NiO is mainly achieved by Ni vacancies.[33,34]

The above-mentioned compositional variation of the defective TMOs have a significant influence on the electronic properties, yet the realistic manipulation of these defects is largely confined into limited ranges. In an attempt to modulate the electronic properties in a wider range, aliovalent doping is applied to control the conductivity of TMOs.[37,38] Donor impurities are used to enhance n-type conductivities with doping cations in a higher valence than the TMO parent ions. The donor cations tend to introduce balancing defects due to the break of stoichiometry and charge balance, in the form of cation vacancies, anion interstitials and electrons. In the example of Nb doped $SrTiO_3$ or $BaTiO_3$, the substitution of Nb^{5+} to Ti^{4+} would introduce balancing electrons into the structure and thus enhance the n-type conductivity.[38,39] The acceptor doping is achieved with cations with lower valence than the parent ions.[40–43] In the example of Sr doped $LaMnO_3$, the substitution of Sr^{2+} to La^{3+} would introduce hole states of mostly Mn 3d characters via promoting Mn^{3+} ($3d^4$) into Mn^{4+} ($3d^3$) in order to keep the charge neutrality.[40,41]

3. Manipulation of functional properties

## 3.1 Ferroelectricity

Ferroelectrics possess a polarization that is spontaneous, stable and electrically switchable.[44] Due to the strong coupling between their electrical, mechanical, and optical responses, ferroelectric materials, especially metal oxides, have been widely investigated for a diverse range of applications such as non-volatile memory devices, sensors, capacitors, non-linear optical components, piezoelectric actuators, energy harvesting and storage, microelectromechanical systems, and high-power electronic transducers.[45–48] Ferroelectricity can be manipulated by the control of defects such as V_O, V_C, defect dipoles, misfit dislocations, grain boundaries and domain walls. V_O are often seen as detrimental to a ferroelectric material, adversely affecting its leakage current and fatigue properties. In the case of

$(LaFeO_3)_2/(SrFeO_3)$ superlattice made up of two nonpolar oxides, however, the introduction of V_O triggers the polar displacement of the Fe ions (Fig. 3a).[49] Bulk $SrMnO_3$ has a paraelectric and G-type anti-ferromagnetic ordering below 233–260 K.[50] When $SrMnO_3$ film is grown on a $(LaAlO_3)_{0.3}(Sr_2AlTaO_6)_{0.7}$ (LSAT) substrate, epitaxial tensile strain ($\sim$1.7%) is accommodated by the creation of V_O, leading to formation of a polar state in this Mn d^0 system.[51] Cation off-stoichiometry defects are also effective in creating and controlling the ferroelectricity. For example, $SrTiO_3$ is an incipient ferroelectric oxide where the ferroelectric order is quenched by quantum fluctuations. The polar nanoregions (PNRs) of nanometer-characteristic size can be naturally formed by the intrinsic Sr vacancies the growth of $SrTiO_3$ film.[52] Lee et al. reported that the electrically induced alignment of these PNRs can create room-temperature ferroelectricity in strain-free $SrTiO_3$ films (Fig. 3b).[9] Further, V_C and V_O can be formed together during synthesis of TMO films. These charged point defect complexes can be defined as defect dipoles due to the strong coupling of electrical and elastic dipoles of such defects to the lattice and polarization. For $BiFeO_3$ thin films, energetically preferred alignment of defect dipoles (V_{Bi} and V_O) parallel to the polarization direction has been demonstrated and used to control the local polarization switching and to achieve the macroscopic double-polarization switching and tri-state memory effects in $BiFeO_3$ films.[53] A similar approach has been applied to ferroelectric $BaTiO_3$ and relaxor ferroelectric $0.68PbMg_{1/3}Nb_{2/3}O_3$-$0.32PbTiO_3$ (PMN-PT) films. Damodaran et al. observed an enhancement of ferroelectric Curie temperature in $BaTiO_3$ films through defect dipoles induced additional anisotropic lattice deformation.[54] Defect dipoles-mediated reversible domain switching can be further used to improve the piezoresponse and realize a large reversible nonlinear electro-strains in $BaTiO_3$ single crystals.[55] Formation and ordering of the defect dipoles can stabilize the direction of polarization against thermal fluctuations, and in turn, weaken the relaxor behavior in PMN-PT films.[56] Due to the formation of V_C and/or V_O, anti-site cationic defects could emerge. For instance, swapping the cation positions between Sr^{2+} and Ti^{4+} to form anti-site defects of Sr_{Ti} or Ti_{Sr}, the paraelectric $SrTiO_3$ becomes ferroelectric at room temperature.[10,57] A similar observation was also reported in anti-ferroelectric $PbZrO_3$, where a nonpolar phase (anti-ferroelectric ordering) is only slightly energetically favorable compared to a polar phase (ferroelectric ordering). The ferroelectric ground state can be stabilized in $PbZrO_3$ films by Pb^{2+} occupying B-site Zr^{4+} positions.[58]

The switching between polarized domains in ferroelectric oxides is mediated by nanoscale defects, such as misfit dislocations and grain boundaries.[14,59–63] Using in situ transmission electron microscopy, Gao et al. found that misfit dislocations can exert a weak pinning force on domain wall motion in $PbZr_{0.2}Ti_{0.8}O_3$ films.[60] Misfit dislocations can also induce polarization instability in $PbZr_{0.52}Ti_{0.48}O_3$ film under compressive strain (Fig. 3c).[59] The flexoelectric effect induced polarization in $SrTiO_3$ has been predicted around misfit dislocations at room temperature. Gao et al. directly observed that stable localized electric dipoles exist near the dislocation
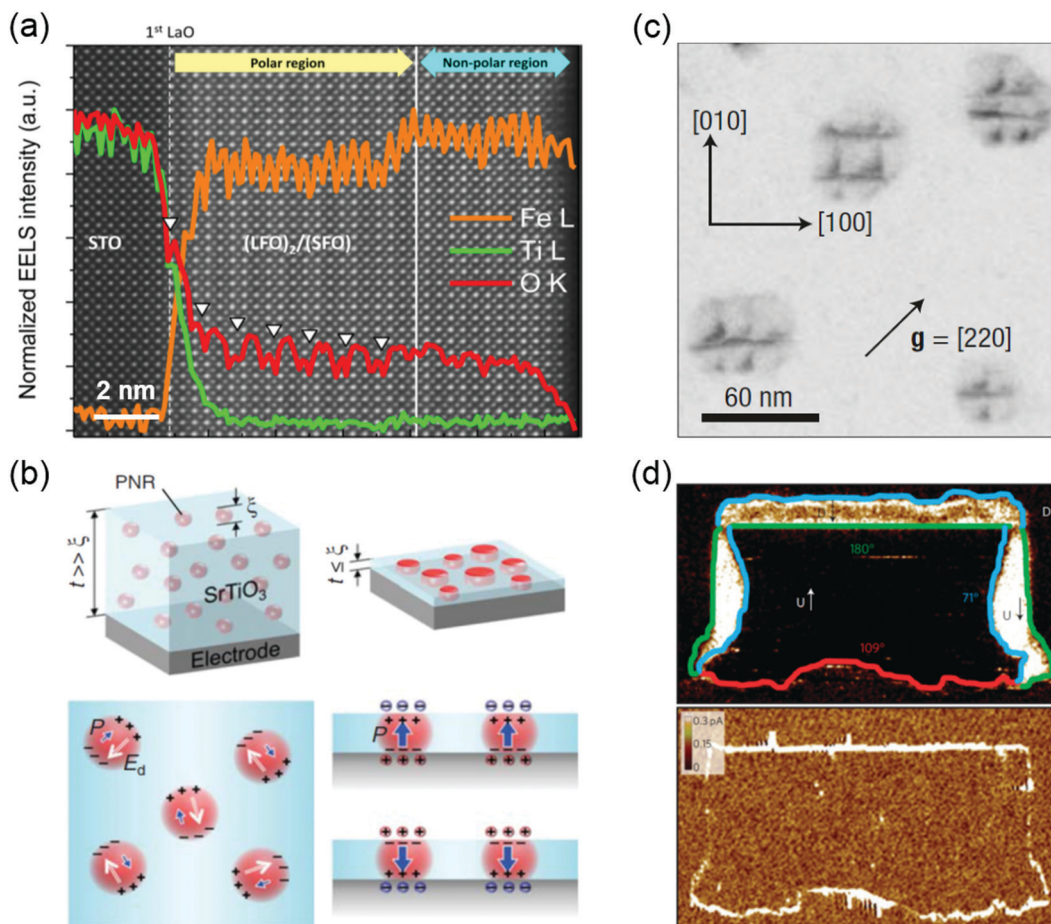
Fig. 3 (a) Core-loss EELS of (LaFeO$_3$)$_2$/(SrFeO$_3$) superlattice showing oxygen vacancy ordering (denoted by white arrows) in a polar region. Reproduced with permission.[49] Copyright 2014 American Chemical Society. (b) Schematic illustration of the effect of size confinement on polar nanoregions (PNR) induced by non-stoichiometry/Sr-deficiency in SrTiO$_3$. Reproduced with permission.[9] Copyright 2015 AAAS. (c) Bright-field plan view image recorded under g = [220] on specimens annealed at 950 °C for 1 h, the dark contrasts showing the network of misfit dislocations. Reproduced with permission.[59] Copyright 2004 Springer Nature. (d) Conductivity at ferroelectric domain walls: PFM phase image (top) and corresponding conductive-AFM image (bottom) of a written domain pattern in a monodomain (~100 nm thick) BiFeO$_3$ film, showing all three types of domain wall, that is, 71° (blue), 109° (red) and 180° (green), and showing conduction at both 109° and 180° domain walls and an absence of conduction at the 71° domain walls. Reproduced with permission.[15] Copyright 2009 Springer Nature.

cores in a 10° small tilt grain boundary in SrTiO$_3$ and further measured the flexoelectric polarization of ~28 μC cm^{-2} at the dislocation core.[14]

When the orientation of electric polarization in ferroelectrics is switched by an applied electric field, this often leads to the appearance of domains of differently oriented regions, separated by domain walls, coexisting in the thin films.[64] Such domain walls become more technologically important as the dimensions of individual elements in electronic devices continue to shrink. Recently, a myriad of novel properties and functionalities have been discovered at domain walls in ferroelectric oxide films, such as BiFeO$_3$. One of these intriguing properties is the enhanced conductivity (1 or 2 orders of magnitude higher) at the domain wall compared to the surrounding domains (Fig. 3d).[15] The origin of domain wall conductivities is still under debate. The lattice distortion and the consequent band gap lowing of domain walls, and the modification of Schottky barrier heights at the heterojunctions

in the regions local to domain walls are the generally accepted mechanisms.[15,65–67] In addition, domain walls can accumulate charged defects, such as Fe^{4+} cations and Bi vacancies in BiFeO$_3$, leading to p-type domain-wall conductivity. An anomalous photovoltaic effect was found at domain walls in BiFeO$_3$ film.[67,68] Furthermore, the observed photovoltaic effect can produce voltages that are significantly higher than the bandgap, and electric-field control of domain wall structure allows the photocurrent to be reversed in direction or turn off.[67,68]

3.2 Magnetism

Magnetic TMOs provide an intellectually rich arena for fundamental scientific discovery and for the invention of faster, smaller, more energy-efficient technologies. V$_O$, V$_C$, grain boundaries, misfit dislocations and BO$_6$ octahedral distortions have been reported as effective methods for changing magnetism. Perovskite manganites of Ln$_{1-x}$A$_x$MnO$_3$ (Ln = La, Pr, Bi; A = Ba, Sr, Ca) have attracted intensive interest because of the fascinating

interplay between spin, charge, orbital and lattice degrees of freedom. The effect of grain boundaries on perovskite manganites has been studied intensively due to its strongly correlation with magnetoresistive (MR) effect.[69,70] Gross et al. found that few nm wide grain boundaries of ferromagnetic $La_{2/3}Ca_{1/3}MnO_3$ film becomes paramagnetic (Fig. 4a),[12] which strongly modifies the transport properties. Besides, experimental and theoretical calculations have shown that V_O can change the hybridized Mn–O–Mn bond and increase the concentration of Mn^{3+} ions, which affect the double exchange interaction and then modify the magnetic properties.[71–73] The transformation from anti-ferromagnetism to ferromagnetism was observed in $YMnO_3$ film by the introduction of V_O.[73] Li et al. reported that oxygen stoichiometry controls the ferromagnetic insulating state in $LaMnO_3$ film,[72] while bulk $LaMnO_3$ shows anti-ferromagnetism. NiO is one of most common natural anti-ferromagnetic oxides the study of which dates back to the dawn of the anti-ferromagnetism.[74] To accommodate the ~7% lattice mismatch between NiO and $SrTiO_3$, high-density dislocations are formed in NiO film grown on a $SrTiO_3$ substrate (Fig. 4b).[11,75] O K-edge electron energy-loss spectra (EELS) show

that the pre-peak around 528 eV is observed only in the spectrum taken at the dislocation core and is attributed to the formation of Ni deficiency. In turn, ferromagnetic ordering of individual dislocations has been discovered in anti-ferromagnetic NiO films.[11]

A layered vacancy ordered brownmillerite (BM) structure can be topotactically transformed from a perovskite structure framework, in which one-sixth of the oxygen anions have been removed. The special feature of this structure-type provides a new pathway for modifying electronic structure (the hybridization between O 2p and TM d orbitals) and then tuning physical properties (magnetic, transport and optical properties) in TMO films.[76,77] Using real-time X-ray diffraction, Cao et al. found the V_O-induced topotactic transition from perovskite (ferromagnetic metal) to BM (anti-ferromagnetic insulator) and vice versa in $La_{0.7}Sr_{0.3}MnO_3$ films (Fig. 4c).[78] During the topotactic phase conversion, an intermediate phase ($La_{0.7}Sr_{0.3}MnO_{2.65}$) was also discovered. A similar topotactic phase transformation has also been observed in $SrCoO_x$, $SrFeO_x$, $LaCoO_x$, and $SrCrO_x$ films.[76,77,79–81] For example, $SrCoO_x$ can experience a phase transition from the perovskite $SrCoO_3$ (P-SCO) to brownmillerite

Fig. 4 (a) High-resolution transmission electron micrographs of a grain boundary in an epitaxial $La_{2/3}Ba_{1/3}MnO_3$ thin film. The dark and bright arrows mark the grain boundary and the crystallographic axis, respectively. Reproduced with permission.[12] Copyright 2000 Elsevier. (b) STEM image of a dislocation core (indicated by the label ⊥ in red) in a NiO thin film. O K-edge EEL spectra measured at the dislocation core and in the bulk region. A peak appears around 526 eV (indicated by the arrow) in the spectrum of the dislocation cores; this is absent in the bulk spectrum. Reproduced with permission.[11] Copyright 2013 Springer Nature. (c) A process schematic for lattice expansion and structure transformation from PV to BM induced by reversible oxygen absorption and desorption. Reproduced with permission.[78] Copyright 2019 Wiley-VCH. (d) Top: STEM image of $LaCoO_3$ film. Middle: EEL spectra: O K edge, Co L_3 edge, and La M_5 edge. Bottom: Theoretical O K absorption edge along with experimental O K and Co $L_{2,3}$ edges for the fully oxygenated CoO_2 planes (red) and the O-deficient planes (blue). Reproduced with permission.[87] Copyright 2012 American Physcial Society. (e) Top: Integrated differential phase-contrast (iDPC) STEM image of $(La_{0.9}Ba_{0.1}MnO_3)_{8uc}/(SrTiO_3)_{8uc}$ (LBMO/STO) superlattice. Middle: plane-averaged octahedral tilt angles of LBMO and STO. Bottom: Ferromagnetic insulating (FMI) state to ferromagnetic metallic (FMM) state transition accompanied by the change of MnO_6 octahedral rotations. Reproduced with permission.[379] Copyright 2020 Wiley-VCH.

$SrCoO_{2.5}$ (BM-SCO) with an increase of V_O concentration.[76] Magnetic properties are simultaneously altered with an increase of V_O concentration due to the change of Co valency, from ferromagnetic P-SCO to antiferromagnetic BM-SCO.[82]

Epitaxial strain, caused by lattice mismatch between the film and substrate, can enhance or suppress the diverse properties of TMO films. To accommodate the lattice mismatch, long-range defect ordering, e.g. V_O, can be formed.[83,84] Coupling between strain and V_O has been widely studied in $LaCoO_3$ films, where long-range ferromagnetic ordering is observed, while bulk $LaCoO_3$ shows no magnetism at low temperature.[85–88] Dark stripes in Z-contrast STEM images have been observed in ferromagnetic $LaCoO_3$ films grown on $SrTiO_3$ substrates (Fig. 4d).[87] Biskup et al. attributed these stripes to V_O ordering, where the dark strips are ferromagnetic insulating regions and significant oxygen deficiency results in the lattice relaxation. This conclusion is based on the fact that there is no significant stoichiometry change for La and Co elements, and there are remarkably reduced O peak intensities in the striped regions observed in atomically resolved electron energy-loss spectroscopy (EELS). However, Choi et al. also reported the dark stripes in Z-contrast STEM images of $LaCoO_3$ films grown on the $SrTiO_3$ substrates and proposed that dark stripes originate from the modulation of the atomic arrangement, caused by the ferroelastic nature of the system, instead of V_O ordering. This conclusion is obtained from there being no significant change in the oxygen non-stoichiometry observed in X-ray absorption spectroscopy.[86] Up to now, it is still not clear whether the ferromagnetism in $LaCoO_3$ film is caused by strain-induced V_O ordering or by strain-induced lattice modulation. When Sr is doped to $LaCoO_3$, V_O are created to neutralize the charge difference between La and Sr. Consequently, dark stripes were observed in $La_{0.5}Sr_{0.5}CoO_3$ films and certainly originated from the formation of V_O ordering.[83]

The fascinating properties of perovskite TMOs are essentially determined by the interlinked and corner-connected BO_6 octahedra, whose bond lengths and bond angles determine the hybridization between TM d and oxygen 2p orbitals, significantly altering the interplay between spin, charge, orbital and lattice degrees of freedom.[89–91] Tuning of the BO_6 octahedra has been widely studied by strain engineering, which changes the c/a ratio for achieving the orbital reconstruction. Using X-ray linear dichroism, Pesquera et al. investigated the orbital reconstruction and the symmetry breaking effect in $La_{2/3}Sr_{1/3}MnO_3$ films and found that the e_g electrons of thick $La_{2/3}Sr_{1/3}MnO_3$ films prefer the $d_{3z^2-r^2}$ orbitals under compressive strain and the $d_{x^2-y^2}$ orbitals under tensile strain.[92] In the case of $(La_{2/3}Sr_{1/3}MnO_3)_n/(BaTiO_3)_n$ superlattice films, through strain engineering and a carefully designed superlattice geometry, the interfacial Mn cations favor the $d_{3z^2-r^2}$ orbitals with $c/a > 1$ while the $d_{x^2-y^2}$ orbitals are stabilized for the inner Mn cations, resulting in an enhancement of ferromagnetic Curie temperature.[93] On the other hand, recent studies demonstrated that oxygen octahedral coupling (OOC) at the hetero-interfaces can delicately tailor the local BO_6 octahedral rotations at an atomic-scale.[94–98,379] Zhai et al. studied the $(LaMnO_3)_n/(SrTiO_3)_m$

superlattices and found that the magnitude of ferromagnetic magnetization is strongly correlated with MnO_6 octahedral rotations.[99] A modulation of the emergent interfacial ferromagnetism was realized in $(CaRuO_3)_n/(CaMnO_3)_m$ superlattices, comprised of an anti-ferromagnet and a paramagnet, through controlling the rotation patterns.[100] The magnetic anisotropy of $La_{2/3}Sr_{1/3}MnO_3$ and $SrRuO_3$ films can also be controlled by engineering the MnO_6 and RuO_6 octahedral rotations,[101,102] respectively. It should be noted that the epitaxial strain also changes the BO_6 octahedral rotations in TMO films.[103] To minimize the strain effect on the changes of BO_6 octahedral rotations and to understand the correlation between the BO_6 octahedral rotations, electronic structure and physical properties in TMO films, Li et al. studied $(La_{0.9}Ba_{0.1}MnO_3)_n/(SrTiO_3)_n$ (only $\sim 0.26\%$ lattice mismatch) superlattices and achieved a long range (up to 12 unit cells) suppression of the MnO_6 octahedral rotations, a preferential occupation of the out-of-plane Mn $d_{3z^2-r^2}$ orbital and a reduced Mn e_g bandwidth in $La_{0.9}Ba_{0.1}MnO_3$. Consequently, a new ferromagnetic insulating state with enhanced Curie temperature of 235 K emerges in $La_{0.9}Ba_{0.1}MnO_3$ (Fig. 4e).[379]

3.3 Multi-ferroelectricity and dielectricity

The ability of multiferroic materials to couple magnetic and ferroelectric orders continues to attract intensive interest because of their potential applications in sensors, spintronics and memory devices.[104–108] Such materials are, however, rare as a consequence of the competing requirements for ferroelectricity and magnetism.[109] Multi-ferroelectricity can be modified or created by domain walls, misfit dislocations, V_O and atomic displacements. Until recently $BiFeO_3$ was the only materials with this functionality at room temperature.[110,111] To relax the misfit strain associated with the lattice mismatch between the $BiFeO_3$ film and the substrate, the formation of crystallographic defects, such as domain walls and dislocations, might occur. Domain walls in multiferroics can manifest a net magnetic moment even if the domains themselves are anti-ferromagnetic or paramagnetic.[112] He et al. reported a strong magneto-resistance in domain walls of $BiFeO_3$ films grown on $DyScO_3$ substrates.[113] Edge dislocations in $BiFeO_3$ films have been observed by scanning transmission electron microscopy.[114] Agrawal et al. found the presence of Bi and Fe atoms in dislocation cores which result in uncompensated Fe spins along the dislocations and give rise to a magnetic signal in $BiFeO_3$ film.[115]

In V_O-ordered brownmillerite $SrFeO_{2.5}$ (anti-ferromagnetic insulator), by controlling the 1D FeO_4 tetrahedral chain network, Kang et al. reported the realization of a room-temperature ferroelectric ferromagnetic in $SrFeO_{2.5}$ film.[116] Li et al. demonstrated that V_O create Ti^{3+} $3d^1$ defect states, mediating the ferromagnetic coupling between the localized Eu $4f^7$ spins, and an increase in the off-center displacement of Ti ions, enhancing the ferroelectric Curie temperature in $Eu_{0.5}Ba_{0.5}TiO_{3-\delta}$ film.[117,118] Similar achievements of ferroelectricity and ferromagnetism was also observed in $YMnO_3$ films by the manipulation of V_O.[73]

Engineering specific atomic displacements or geometric design has been applied to design a single-phase multiferroic. Hexagonal $LuFeO_3$ is a geometric ferroelectric with the greatest known planar rumpling.[119] In the $(LuFeO_3)_m/(LuFe_2O_4)_1$ superlattices, Mundy *et al.* introduced the individual monolayers of FeO during the growth to construct formula-unit-thick layers of ferromagnetic $LuFe_2O_4$ within the $LuFeO_3$ matrix and further demonstrated that the severe rumpling imposed by the neighbouring $LuFeO_3$ enhances the magnetic transition temperature of $LuFe_2O_4$ to 281 K and also drives $LuFe_2O_4$ into a ferroelectric state (Fig. 5a).[120] Moreover, electric-field control of magnetism has been realized at 200 K. Through the engineering of octahedral tilts, room-temperature ferroelectric ferromagnetic and magnetoelectric coupling have been realized in $(Ca_ySr_{1-y})_{1.15}$-$Tb_{1.85}Fe_2O_7$.[121] Choi *et al.* and Chen *et al.* reported room-temperature multiferroic films based on two partially miscible phases of $BiFeO_3$ and $BiMnO_3$.[122,123]

Dielectric materials exhibiting temperature- and frequency-stable permittivity as well as dielectric tunability and sufficiently low dielectric loss, continues to arouse considerable interest motivated by their myriad device miniaturization and high-energy-density storage application.[124,125] Dielectricity can be tuned by V_O, V_C, misfit dislocations and dipolar defects. Lee *et al.* demonstrated that the presence of $(SrO)_2$ crystallographic shear planes in $Sr_{n+1}Ti_nO_{3n+1}$ film provides a means of locally accommodating non-stoichiometry (Sr vacancies), which

significantly reduces the dielectric loss and achieves the dielectric tunability (20% at 50 kV cm^{-1}) across the entire microwave range (Fig. 5b).[126] Vertically aligned nanocomposites (VANs) with ordered vertical heterointerfaces provide an effective platform to tune the dielectric properties. Lee *et al.* studied the dielectric tunability in $Ba_{0.6}Sr_{0.4}TiO_3:Sm_2O_3$ VAN films and reported the achievement of a low dielectric loss ($\tan\delta < 0.1$) and high and stable dielectric tunability (75% at 200 kV cm^{-1}) at room temperature.[127] A very low dielectric loss ($\tan\delta \sim 0.01$) and relative large dielectric tunability (49% at 400 kV cm^{-1}) was further reported in $SrTiO_3:Sm_2O_3$ VAN film.[128] Yang *et al.* explored $BiFeO_3:Sm_2O_3$ VAN films and found that dielectric loss and leakage current were reduced compared to plain $BiFeO_3$ films (Fig. 5c).[129,130] The increased vertical interfacial area and reduced V_O in the $BiFeO_3$ phase are responsible for these improved properties. Enhanced ferroelectric Curie temperatures and reduced leakage current were also reported in $BaTiO_3:Sm_2O_3$ VAN films.[131,132] Li *et al.* found that the misfit dislocations are formed at the vertical interface due to a large vertical lattice strain. The movement of V_O is confined at the vertical interface and hampered by the misfit dislocations, which contributed to a relaxation behavior in $BaTiO_3:Sm_2O_3$ VAN film.[133] Dipolar defects are created by the change of V_O concentration and further interact with the off-centered Ti ions, which results in dielectric relaxation in $Eu_{0.5}Ba_{0.5}TiO_{3-\delta}$ films.[134]
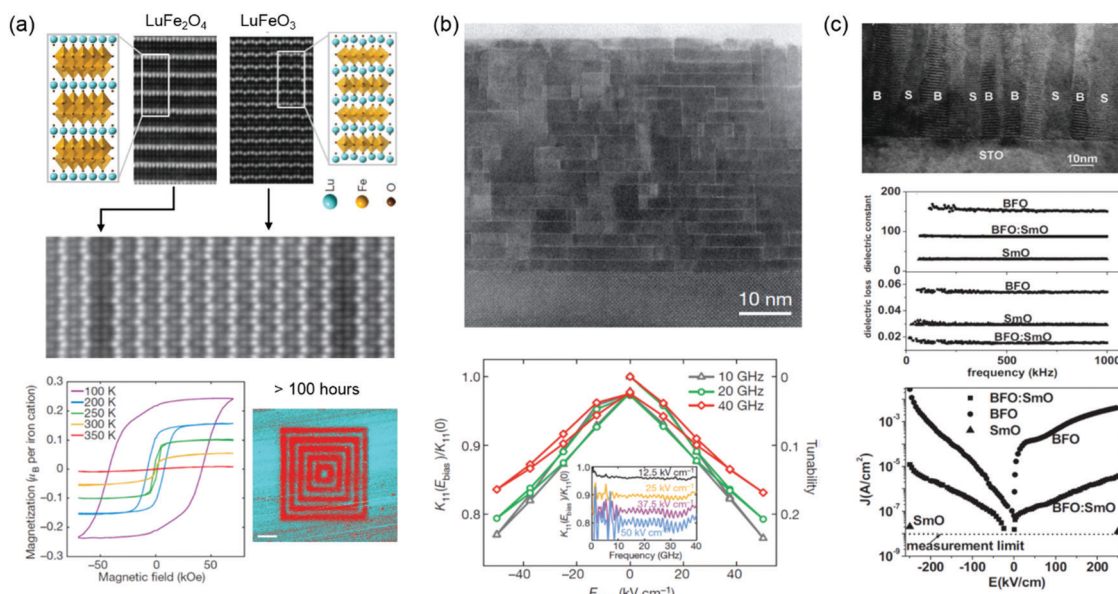
Fig. 5 (a) HAADF STEM images of top: end-members $LuFe_2O_4$ (left) and $LuFeO_3$ (right); middle: $(LuFeO_3)_9/(LuFe_2O_4)_1$ superlattice film. Bottom left: Loops of the magnetization as a function of the magnetic field for the $(LuFeO_3)_9/(LuFe_2O_4)_1$ superlattice. Bottom right: Out-of-plane PFM image of the $(LuFeO_3)_9/(LuFe_2O_4)_1$ superlattice. Reproduced with permission.[120] Copyright 2016 Springer Nature. (b) Bright-field STEM image of epitaxial $Sr_{n+1}Ti_nO_{3n+1}$ ($n = 6$) film grown on $DyScO_3$. The ratio of K_{11} under an applied bias field (E_{bias}) to that at zero bias field (left-hand axis) and tunability (right-hand axis) of the $n = 6$ sample at several different frequencies in the microwave range. The inset shows the dielectric constant ratio as a function of frequency for several values of applied E_{bias}. Reproduced with permission.[126] Copyright 2013 Springer Nature. (c) Top: A cross-sectional TEM image of a BFO:SmO VAN film with vertical nanocolumns of BFO and SmO (B represents BFO, and S represents Sm_2O_3) Middle: Frequency-dependent dielectric constant and dielectric loss of BFO:SmO VAN thin films, compared to BFO and SmO single-phase thin films. Bottom: Leakage current density *versus* electric field (J–E) characteristics of BFO:SmO, BFO, and SmO thin films. Reproduced with permission.[129] Copyright 2009 Wiley-VCH.

3.4 2DEG and 2DHG

The emergence of conducting interface can be promoted by polar discontinuities. Ohtomo *et al.* reported the discovery of a two-dimensional electron gas (2DEG) at the LaAlO$_3$/SrTiO$_3$ heterostructures based on this idea.[135] Both compounds are band insulators (E_{gap} = 5.6 eV for bulk LaAlO$_3$ and E_{gap} = 3.2 eV for bulk SrTiO$_3$). However, when a LaAlO$_3$ layer is deposited layer-by-layer on top of a (001) TiO$_2$-terminated SrTiO$_3$ substrate, the interface switches to a metallic state when the LaAlO$_3$ layer thickness exceeds 3 unit cells.[136] These experimental observations have generated a lot of interest in the SrTiO$_3$-based interfaces,[137,138] due to their potential applications in novel electronic devices and rich physics arising from the complex electronic correlations.[139–141] Although significant attempts have been paid to understand the LaAlO$_3$/SrTiO$_3$ interface, the origin of interfacial conductivity is still under debate. From the very beginning, the conductivity observed at the LaAlO$_3$/SrTiO$_3$ interface was attributed to the polar discontinuity.[135] This polar catastrophe scenario emerges from a simple valence counting consideration. As shown in Fig. 6a, the TiO$_2$ and SrO planes are neutral, however, the LaO and AlO$_2$

layers are polar and carry a positive and negative charge of +1 e and −1 e per unit cell, respectively. The diverging electric potential can be compensated by electron transfer from LaAlO$_3$ to the interfacial SrTiO$_3$ layer with the formation of the n-type interface. The polar catastrophe picture explains many of the features of the electron gas at the LaAlO$_3$/SrTiO$_3$ interface, in particular the existence of a critical thickness for the onset of metallic behavior. However, some unresolved inconsistencies between theories and experiments still exist. For example, the predicted sheet carrier densities and their variation with LaAlO$_3$ thickness have not been observed in experiments yet.[136,142]

Besides the polar discontinuity, the defects (*e.g.*, V$_O$) and cation intermixing are also invoked to understand interfacial conductivity.[143,144] It was found that charge transport depends sensitively on the growth conditions, especially on the oxygen pressure P_{O_2}, indicating that V$_O$ could be an alternative doping mechanism.[135,145–147] Temperature-dependent sheet resistance R_{sheet} depends dramatically on the growth pressure (Fig. 6b). For $P_{O_2} \sim 10^{-6}$ mbar, the observation of a larger carrier density originates from the doping of V$_O$ to the SrTiO$_3$ substrate. For
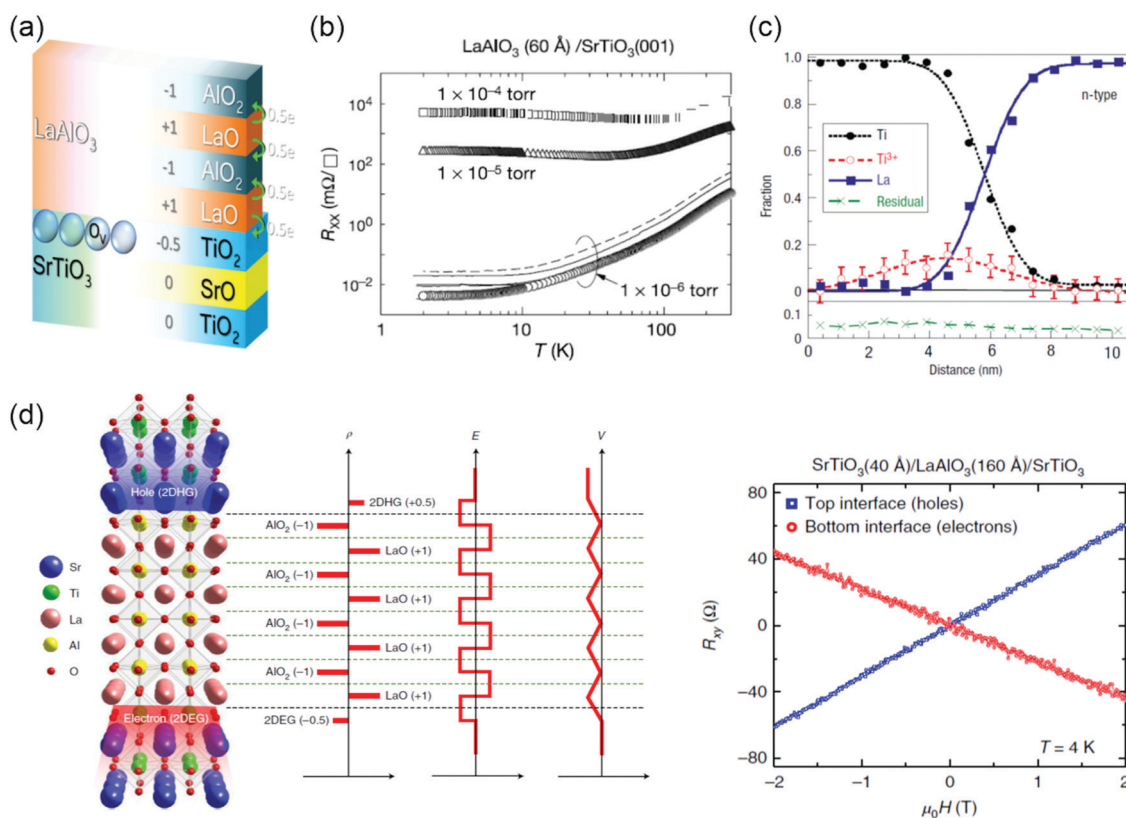
Fig. 6 (a) Sketch of two mechanisms, polar discontinuity and oxygen vacancies, for inducing mobile electrons at the LaAlO$_3$/SrTiO$_3$ interface. Reproduced with permission.[3,378] Copyright 2018 Wiley-VCH and Copyright 2013 American Physcial Society. (b) Temperature-dependent sheet resistance R_{xx} for the interface between LaAlO$_3$ and SrTiO$_3$. Reproduced with permission.[135] Copyright 2004 Springer Nature. (c) AlO$_2$/LaO/TiO$_2$ interface showing the fractions of elemental Ti and La from the Ti-L and La-M edges, as well as the Ti^{3+} fraction determined from a least-squares fit to the Ti-L edge from Ti^{3+} and Ti^{4+} reference spectra. There is excess Ti^{3+} on the substrate side of the interface. Reproduced with permission.[149] Copyright 2006 Springer Nature. (d) Left: Schematics that depict the electronic reconstruction across the oxide heterostructure. Right: Hall resistance R_{xy} *versus* magnetic field μ_0H for the top and bottom interfaces at 4 K. The top interface clearly shows a positive slope, which indicates p-type conductivity, whereas the bottom interface shows a negative slope, which indicates n-type conductivity. Reproduced with permission.[150] Copyright 2018 Springer Nature.

P_{O_2} between 10^{-4} and 10^{-2} mbar, the observation of conductivity is believed to be confined to the interface. When the P_{O_2} is above 10^{-2} mbar, the reported results are more diversified, such as insulating, superconducting and magnetoresistance effects.[147,148] Atomic-resolution electron energy loss spectroscopy (EELS) revealed that the interface is not chemically sharp, with some La/Sr and Ti/Al intermixing included (Fig. 6c).[149] Such chemical doping could also be the source of the carriers at the interface, with the interface layer behaving as a $La_{1-x}Sr_xTiO_3$ film, which are responsible for the interfacial conductivity. Recently, Lee et al. reported the observation of a two-dimensional hole gas (2DHG) in (001) $SrTiO_3/LaAlO_3/SrTiO_3$ heterostructures (Fig. 6d).[150] The $SrTiO_3$ substrate is terminated at TiO_2. Depth-resolved cathodoluminescence spectroscopy (DR-CLS) was used to support that the formation of 2DHG is not attributed to the V_O.

The fundamental questions on the origin of the carrier, the carrier density, the shape of the confining potential and the role of electronic correlations are too complicated and still can't be answered at the $LaAlO_3/SrTiO_3$ interface and other similar systems. More comprehensive discussions can be found in other review papers.[3,151–153]

3.5 Metal–insulator transitions

Understanding metal–insulator transitions in strongly correlated materials is one of the major challenges in condensed matter physics,[154–158] with implications for both fundamental science and technology.[159,160] Strain, V_O and BO_6 octahedral distortions have been applied for manipulating metal–insulator transition behaviour. An archetypal correlated material is VO_2, showing a pronounced metal–insulator behavior from low-temperature insulating monoclinic (M1) phase to high-temperature metallic rutile (R) phase near room temperature (341 K in bulk).[161] Epitaxial strain and V_O defects have been widely used in order to control metal–insulator transition dynamics for achieving a shape phase transition in VO_2 epitaxial films.[162–166] Using electrolyte gating with an ionic liquid, Jeong et al. reported that the suppression of the metal–insulator transition in VO_2 film is achieved by electric field-induced V_O formation for reducing the valence state of V^{4+} to V^{3+} (Fig. 7a).[167] However, creation of V_O by ionic liquid gating is possibly linked with both hydrogen intercalation whence a trace of water remains in the ionic liquid and degradation of the entire film under high electric field.[164,168] By growing the $VO_{2-\delta}/VO_2$ bilayer films on TiO_2 substrates, Lee et al. found that an interface interaction between $VO_{2-\delta}$ and VO_2 can suppress the electronic correlations for controlling the metal–insulator transition.[169] By annealing VO_2 films at an ultralow oxygen partial pressure ($P_{O_2} \sim 10^{-24}$ atm), the formation of V_O led to a change of the band structure (Fig. 7b) and an appearance of a metallic state down to 1.8 K.[165] Moreover, the VO_2 film can revert back to its original state by a simple annealing process in oxygen.

As discussed above, during the transformation of a layered V_O ordered brownmillerite structure to a perovskite structure framework, the modification of electronic structure, such as the hybridization between O 2p and TM d orbitals, is responsible for the reversible change between the brownmillerite insulating state and the perovskite metallic state. This phenomenon has been widely observed in $La_{0.7}Sr_{0.3}MnO_{3-x}$, $SrCoO_x$, $SrFeO_x$, $LaCoO_x$, and $SrCrO_x$ films.[76–81] Taking $SrFeO_x$ as an example, $SrFeO_{2.5}$ exhibits insulating (or semiconducting) behaviour in the BM structure while $SrFeO_3$ shows metallic behaviour in the perovskite structure. By using different growth atmospheres (oxygen partial pressure) or by modifying the interfacial strain by changing the growth substrates, V_O concentration could be successfully controlled and could therefore modulate the conductivity and metal–insulator transition.[81,170]

The properties of perovskite rare-earth nickelates, $RNiO_3$ (R = La–Lu), have been attracting enormous attention owing to a rich temperature-composition phase diagram including a metal-to-insulator phase transition coinciding with a nickel charge ordering.[16,171,172] The origin of the metal-to-insulator transition has been widely debated in the literatures.[173–176] The unoccupied states at the bottom of the conduction band have substantial oxygen character, corresponding to an oxygen

Fig. 7 (a) Sheet resistance *versus* temperature for various gate voltages varying from 0 to 1.8 V for VO_2/(001)TiO_2. Reproduced with permission.[167] Copyright 2013 AAAS. (b) Schematic illustration of the band structure of pristine VO_2 in the insulating state (top) and metallic state (bottom left), while the band structure of oxygen-deficient $VO_{2-\delta}$ is shown in bottom right, where strong charge filling in the π^* and $d_{\parallel}$ orbitals occurs. Reproduced with permission.[165] Copyright 2017 American Physical Society. (c) Temperature-dependent resistivity of $(LaFeO_3)_1–(SmNiO_3)_n$ superlattices and 30 uc $SmNiO_3$ film. Reproduced with permission.[183] Copyright 2018 National Academy of Sciences.

ligand hole consistent with a negative charge transfer character for the system.[177] In a non-disproportionated structure, the nickel sites have nominal valence 3+ and the oxygen ligand holes are distributed equally among all of the NiO_6 octahedra, resulting in a $d^8\underline{L}$ configuration, where $\underline{L}$ denotes an oxygen ligand hole. V_O in the rare-earth nickelates can modify the electronic structure and act as electron donors. The added electron can be regarded as converting nickel from 3+ to 2+, or as converting the nickel site in the NiO_6 octahedron from $d^8\underline{L}$ to d^8. This results in a large on-site bandgap stemming from the electron–electron correlations and the crystal field splitting. As a result, metal–insulator transitions of $LaNiO_3$, $NdNiO_3$ and $SmNiO_3$ films can be controlled by the formation of V_O.[178–181] Recently, Mercy et al. identified that the breathing mode responsible for the metal–insulator transition in the perovskite nickelates is triggered by NiO_6 octahedral rotations and tilts.[182] Based on this idea, in the case of the $(LaFeO_3)_1/(SmNiO_3)_n$ superlattices, Liao et al. demonstrated that the metal–insulator transition in the $SmNiO_3$ layer can be adjusted by the modulation of NiO_6 octahedral tilt (Fig. 7c).[183]

3.6 Resistive switching

Resistive random-access memory (RRAM or ReRAM) is one of the most promising emerging devices for logic-in-memory operations, attracting great attention due to the possibility of high-density integration, plausible scalability, ultra-fast access time, low power consumption and ease of fabrication. ReRAMs can be divided into two categories: electrochemical metallization cells ReRAMs – also called conductive bridge random access memories – and valence change mechanism ReRAMs – also called redox random access memories ReRAMs.[184,185] Resistive switching behaviour can be manipulated by controlling cations, V_O and interfaces. In electrochemical metallization cells, a nanoscale conductive metallic path between a working electrode/anode (often electrochemically active, such as Ag or Cu) and a counter electrode/cathode (often inert, such

as Pt, Au or TiN) is formed or broken by the generation, movement and reduction of mobile metal cations (i.e., Ag^+ or Cu^{2+}).[186,187] Valence change mechanisms occur in a wide range of TMOs.[188,189] In TMOs, anions such as oxygen ions (or, equivalently, V_O) are more mobile than the cations when they are thermally and/or electrically activated. Therefore, understanding how the resistance of TMOs is influenced by V_O is very important. Generally, V_O will affect the resistance and contribute toward the introduction of resistive switching phenomena in one of three ways: (1) V_O tend to cluster and generally form filamentary shapes under an electric field (Fig. 8a).[190–192] When such clusters are formed, the resistance of the local region becomes much lower than that of the surrounding oxide matrix, and the low-resistance state (LRS) and high-resistance state (HRS) will therefore be determined by the creation and rupture of the conducting filaments (CFs), respectively. (2) V_O can control the Schottky barrier characteristics.[188,193] In a typical capacitor sample geometry, an interface is formed between the metal electrode and the TMOs films. Depending on the difference of work functions between the metal electrode and the TMOs, a Schottky barrier can be formed. Under an external bias, the distribution and density of V_O can vary, which affects the height and width of the Schottky barrier and leads to a change in the resistance of the sample. (3) V_O can also form trap sites for electrons inside the Schottky barrier region.[193–195] In this situation, the Schottky barrier can be modulated by the neutralization of the V_O due to the trapping of electrons, inducing resistive switching phenomena.

Resistive switching devices are normally in the form of metal-dielectric-metal two-terminal junctions. The interface between metal electrode and the TMOs films plays a critical role in the resistive switching. Using vertical heterointerfaces in vertically aligned nanocomposite (VAN) films for studying resistive switching has been reported. Different from lateral heterostructures, VANs exhibit a much higher density of vertical interfaces which can be used for improving resistive

Fig. 8 (a) High-resolution transmission electron microscopy (HRTEM) image of a nanocrystalline Ti_4O_7 (Magnéli phase) filament with a conical shape (outlined in blue) in a $Pt/TiO_2/Pt$ anion-type RSM device. Reproduced with permission.[190] Copyright 2010 Springer Nature. (b) Top: Spontaneous phase ordering of $SrTiO_3$ and Sm_2O_3 in a cross-sectional TEM image. Bottom: HRTEM image of the vertical interface between a $SrTiO_3$ matrix and Sm_2O_3 nanocolumn. Atomic arrangement at the vertical interface can be crystallographically modelled. Reproduced with permission.[196] Copyright 2014 Wiley-VCH. (c) Sketch (top) and SEM (bottom) image of a nanoparticle-on-mirror (NPoM) memristive cell. Reproduced with permission.[198] Copyright 2016 Wiley-VCH.

switching. Lee *et al.* reported that due to the structural incompatibility of $SrTiO_3$ and Sm_2O_3, the possible formation of V_O was found at vertical heterointerfaces.[196] The Joule heating-accelerated drift of V_O localized at vertical heterointerfaces reduces the wide fluctuation in switching parameters (Fig. 8b). In self-assembled Sm-doped CeO_2 and $SrTiO_3$ VAN films, large on–off ratios and high reproducibility were achieved by the separate tailoring of nanoscale ionic and electronic channels.[197]

Although great progresses have been made in valence change mechanism ReRAMs, mastery of the conduction mechanism is still incomplete. To identify and understand failure mechanisms, characterization methods, such as voltage-sweep and voltage-pulse measurements, electrochemical cyclic voltammetry, and *ex situ* and *in situ* electron microscopy have been used. However, limited success is achieved in fully understanding the switching dynamics. Recently, a spectroscopic technique to optically characterize *in situ* resistive switching effect was reported.[198] Resistive switches arranged in a nanoparticle-on-mirror (NPoM) geometry were developed, exploiting the high sensitivity to morphological changes occurring in the tightly confined plasmonic hotspot within the switching materials (Fig. 8c).[198] This provides a non-destructive technique to understand the switching dynamics.

Recently published reviews provide more comprehensive discussions on classification of resistive switching phenomena/mechanisms, other microscopic origins of resistive switching in TMOs, resistive switching related technological issues (*e.g.*, fluctuation, sneak-paths and multilevel switching) and neuromorphic computing based on resistive switching which has drawn extensive attention due to its promising capability in processing massive data in the Internet of Things and big-data workloads.[199–203]

3.7 Ionic conductivity

One of the leading technologies for future power generation is the solid oxide fuel cell (SOFC).[204–206] One important challenge in improving SOFC technology is to reduce the working temperature to 500–700 °C. Over several decades, developing new electrolyte materials with high ion conductivity has been the primary activity. The oxygen diffusivity (D) scales almost linearly with V_O concentration when the value of V_O is low. On the other hand, oxygen diffusion is a thermally activated process where D can be described by the Boltzmann relationship as $D = D_0 \exp\left(\frac{-E_m}{k_B T}\right)$, where D_0 is a constant and E_m denotes migration enthalpies or energy barrier along this path. Compared to linear relationship between D and V_O concentration, D changes exponentially with E_m which makes it a critical parameter to reduce.[206] The oxygen migration energy can be modified by misfit dislocations, V_O, elastic strain, BO_6 octahedral distortion, and so on.

Yttria-stabilized zirconia (YSZ) is the material mostly used in SOFCs because of its mechanical stability, chemical compatibility with electrodes, and high oxygen ionic conductivity. Engineering misfit dislocation and V_O at heterogeneous interfaces have been used to improve the charge-carrier density and enhance the ionic conductivity. For example, Garcia-Barriocannal *et al.* reported an eight-orders-of-magnitude enhancement of YSZ conductivity in epitaxial multilayers consisting of two unit cell YSZ and thick $SrTiO_3$, which attributes colossal enhancement of ionic conductivity to either V_O or O disorder in the interfacial plane.[207] Density-functional calculations revealed that colossal ionic conductivity in $YSZ/SrTiO_3$ multilayers can be explained in terms of lattice-mismatch strain and O-sublattice incompatibility at the interface (Fig. 9a).[208] However, these experimental results still have to be independently verified, as there are some debates as to whether the conductivity of $YSZ/SrTiO_3$ multilayers is purely ionic.[209] Sillassen *et al.* reported that interfacial effects dominate the conductivity at the low temperature (< 350 °C), showing more than three orders of magnitude enhancement in YSZ films compared to bulk YSZ.[210] The observed enhancement in lateral ionic conductivity is caused by a combination of misfit dislocations and elastic strain at the interface (Fig. 9b and c). Similar evidences for misfit dislocations related to fast ion conduction in lateral heterostructures are reported in numerous experimental and theoretical studies.[211–215]

Vertically aligned nanocomposite (VAN) films have been also developed to improve the ionic conductivity and design state-of-the-art ionic devices.[216,217] Compared to the oxygen ion diffusion along lateral interface direction in the lateral heterostructures, VANs allow fast oxygen ion transport along the out-of-plane direction which is the favored charge flow direction of SOFCs. Enhanced ionic conductivity values by over 2 orders of magnitude, compared to plain YSZ films, was reported in $YSZ:SrTiO_3$ VAN films (Fig. 9d).[218] The improved crystallinity of YSZ nanocolumns in VAN film was proposed to explain the enhanced ionic conductivity. Similar to $YSZ:SrTiO_3$ VAN films, the enhancement in vertical ionic conductivity has been also demonstrated in VAN systems of $YSZ:GDC$[218] (Gd-doped CeO_2) and $SrTiO_3:SDC$ (Sm-doped CeO_2).[219]

Very recently, Gao *et al.* reported that, through the creation of $La_{0.9}Sr_{0.1}Ga_{0.95}Mg_{0.05}O_{3-\delta}/DyScO_3$ superlattice films, both expanded unit-cell volume and large octahedral rotations can be realized in $La_{0.9}Sr_{0.1}Ga_{0.95}Mg_{0.05}O_{3-\delta}$ (LSGM), which shows an enhancement of ionic conductivity (Fig. 9e).[220] This provides a new pathway for the rational design of ion-conducting perovskite electrolytes *via* controlling BO_6 octahedral rotations.

3.8 Photo-electrocatalyst and electrocatalysts

Electrochemical water splitting to produce storable hydrogen (also referred to as "solar fuel") driven by solar energy or by electricity from renewable energy (*e.g.*, photovoltaics) is widely seen as a promising pathway towards a globally sustainable energy future. The key to enabling these approaches is the development of abundant, low-cost, stable semiconductor materials to harness solar energy and efficient electrocatalysts to accelerate the water oxidization reaction.[221] Complex TMOs are appealing materials for these purposes, owing to their earth-abundance, good stability and tunable physicochemical properties *via* doping and defect engineering (especially V_O, V_C and lattice distortions).[222–224]
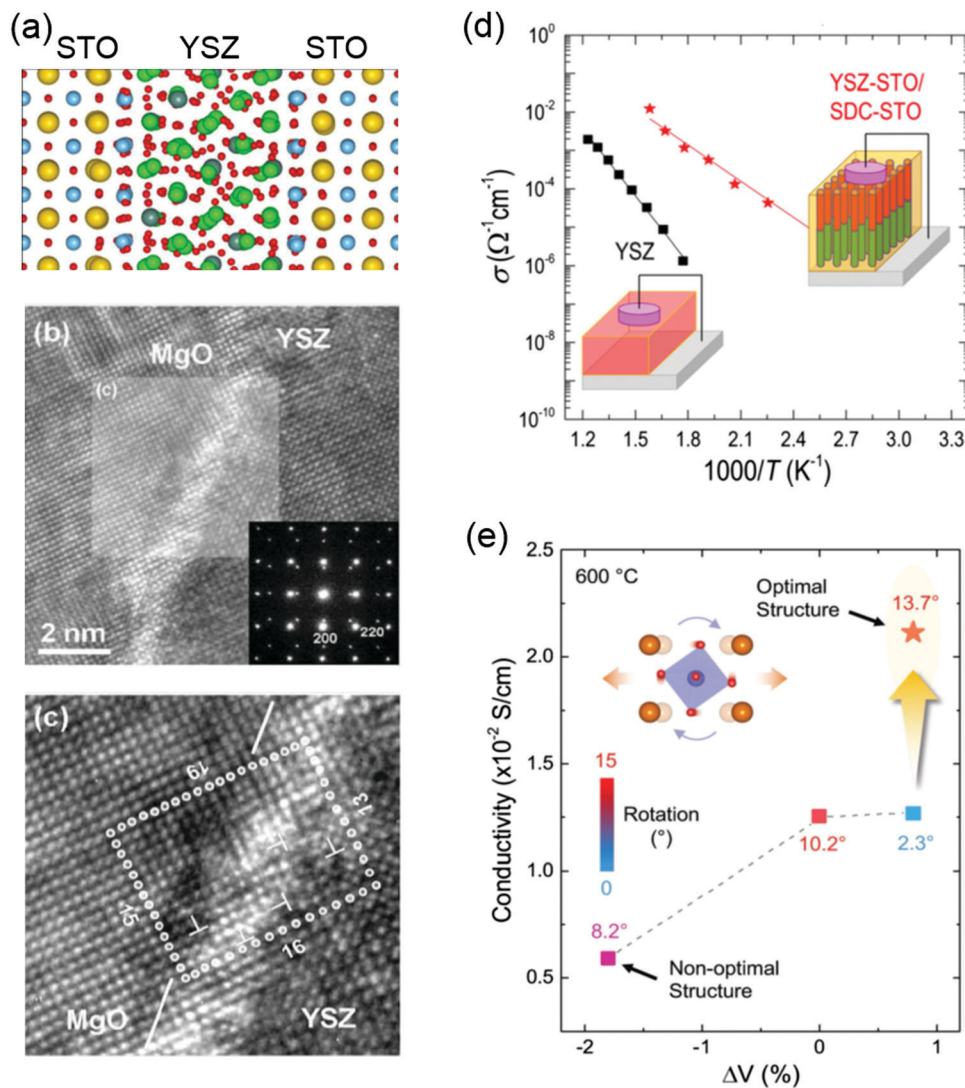
Fig. 9 (a) Structure of the 1 nm YSZ layer sandwiched between layers of STO at 360 K. Sr atoms are shown as large yellow balls, Ti in blue, Zr in green, Y in gray, and O in red. Reproduced with permission.[208] Copyright 2010 American Physical Society. (b) HRTEM image of the YSZ/MgO interface region. The inset shows the SAED pattern across the YSZ/MgO interface along the YSZ (100) direction. Reproduced with permission.[210] Copyright 2010 Wiley-VCH. (c) Magnification of the area marked in (b). Misfit dislocations are indicated by T symbols. (d) Ionic conductivity of plain YSZ films compared to YSZ-STO VAN films. Reproduced with permission.[218] Copyright 2015 American Chemical Society. (e) Ionic conductivity as a function of unit-cell volume and octahedral rotation angles for LSGM. Reproduced with permission.[220] Copyright 2020 Wiley-VCH.

To achieve effective implementation of solar driven photoelectrochemical water splitting (PEC), stringent requirements on the material properties should be satisfied, including an appropriate bandgap for sufficient light absorption, adequate band edge potentials to drive redox reactions, favorable carrier diffusion length to ensure the effective progress of the interface reaction. TMO semiconductors such as TiO_2, Fe_2O_3 and $BiVO_4$ have attracted intensive attention for the last decades.[225–228] However, their PEC performance is still far from the standard of practical applications, because of limitations in materials properties. For example, TiO_2 has a much too large bandgap (3.0–3.2 eV) for visible light absorption.[229,230] Fe_2O_3 has a low bandgap of $\sim$ 2.1 eV, but is inherently limited by its low electrical conductivity, short diffusion length (2–4 nm) and lifetime (<10 ps) of photoexcited carriers.[231,232]

Doping, alloying and defect engineering are widely used as strategies to enhance the PEC activity with the purpose of: (i) decreasing the bandgap for efficient visible light absorption and (ii) optimizing the carrier transport. Doping can introduce extra energy levels within the bandgap (for example, Bi^{3+} $6s^2$ state hybrid with Ti^{4+} d^0 orbital) to narrow the bandgap value.[233] On the other hand, it has been shown that Fe_2O_3 can be p-type doped by divalent cations such as Mg^{2+},[234,235] and n-type doped with tetravalent cations such as Ti^{4+}, Sn^{4+}, *etc.*[236–239] Doped Fe_2O_3 can remarkably enhance the PEC activity toward water oxidation compared with undoped counterparts.[239–242] The same trend of enhanced PEC activity was also achieved in Mo^{6+} or W^{6+} doped $BiVO_4$.[243–246]

Defect engineering is another approach to tuning the band structure and therefore PEC performance of TMOs, especially

V_O, V_C, and lattice distortion. V_O provide donor states to increase n-type conductivity, while V_C provide acceptor states for p-type conductivity.[247,248] Furthermore, the defects also provide favorable absorption sites for chemical reactions to enhance the activity. Cui *et al.* prepared black TiO_2 nanotubes (B-TNTs) with abundant V_O *via* the Al reduction method, which shows 5 times higher applied bias photon-to-current efficiency (ABPE) than that of TNTs and a larger visible light photo-response region from 400 nm to 460 nm.[249] The new donor level at about 0.7 eV below the conduction band minimum (CBM) corresponding to the formation of V_O.[250] Yim and coworkers attribute the bandgap state in TiO_2 (110) to bridging V_O by ultraviolet photoemission spectroscopy and scanning tunneling microscopy.[251] But the contribution of interstitial Ti is also proposed in another work.[252] Because of the increased carrier density and the lowered activation energy for charge transport, the separation and migration of photo-excited carriers can be effectively improved. However, excess V_O may trap photo-electrons and act as recombination centers, and then decrease the photocurrent.[253] The above effects also hold for $BiVO_4$.[254,255]

Furthermore, the presence of V_O has the ability to work as active site for PEC water splitting and enhance the adsorption energies of H_2O_{ads}, OH_{ads}, and O_{ads} (Fig. 10a).[256] The strong interaction indicates that an increased overlap between Bi 6s, V 3d and O 2p orbitals, and then accelerates the hole transfer at electrode/electrolyte interface.

The oxygen reduction reaction (ORR) and OER are the essential processes for water splitting, fuel cell, and metal–air batteries. However, the ORR and OER process involve four electron transfer processes with sluggish reaction kinetics. Precious Pt and Ir based electrocatalysts are needed, limiting its large-scale utilization. Low-cost TMOs electrocatalysts such as Co_3O_4, NiO, $LaNiO_3$, $La_{1-x}Sr_xCoO_{3-\delta}$, *etc.*, have been developed in the past few decades.[257–260] The presence of defects significantly affects the band structure of catalysts and the local bond environment of defect sites, and hence manipulates the adsorption sites, energy, and configuration of the reactant or various intermediate species.[261–263] Ling *et al.* synthesized CoO nanorods with oxygen-terminated {111} facets, where contain a large number of O-vacancies.[264] It is worth mentioning that an additional state of hybridization of O 2p, Co-3d and Co 3s appears in the bandgap when introducing V_O, which results in the lowest adsorption energies of intermediates on active sites, as shown in Fig. 10b. During the reaction process, owing to $|\Delta G_{OOH^*}| \approx |\Delta G_{O^*}| \approx |\Delta G_{OH^*}| \approx 0$, that the {111}-$V_O$ surface can adsorb and desorb easily. Based on the single-crystalline ultrathin Co_3O_4 model, it was able to further discuss the effect of defects on electrocatalytic performance by introducing vacancies into specific crystal facets.[265] The Co_3O_4 {111} surface with rich V_O exposed second-layered Co sites and then these Co atoms become the active sites under the influence of neighboring O atoms. This structure exhibits a low overpotential
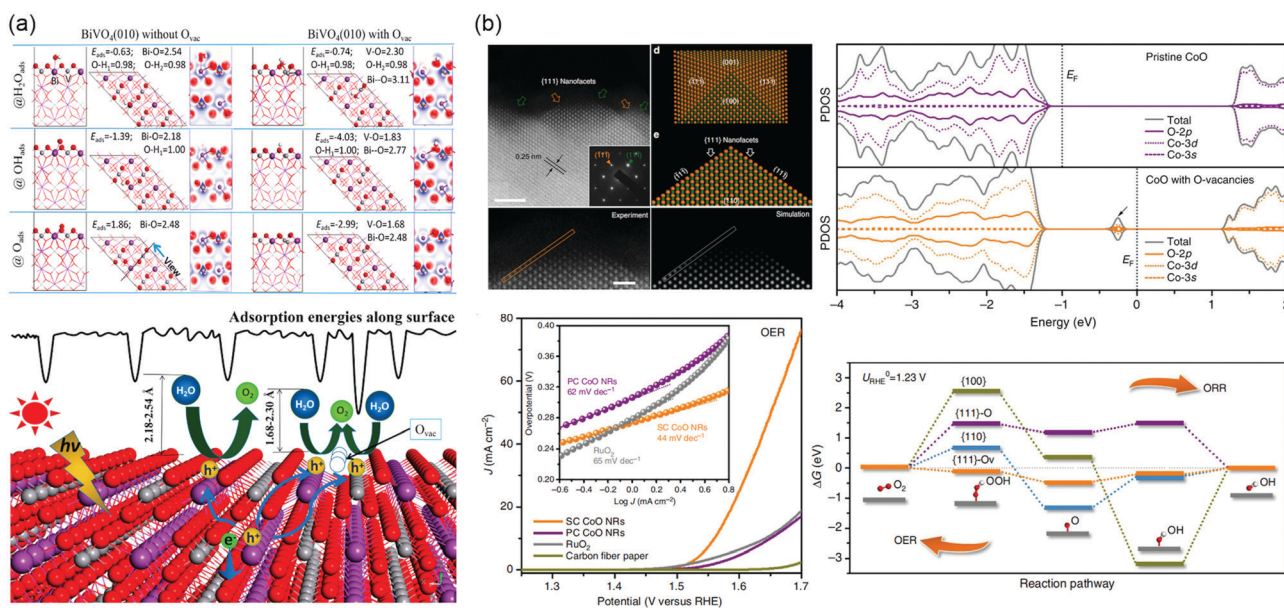
Fig. 10 (a) Top: Adsorption structures, energies and electron density difference of H_2O_{ads}, OH_{ads} and O_{ads} involved in a water splitting process on $BiVO_4$ (010) facet with O_{vac}. Bottom: Schematic picture of the PEC water splitting process on $BiVO_4$ (010) facet with or without O_{vac}. Adsorption energy along surface is illustrated. Reproduced with permission.[256] Copyright 2017 American Chemical Society. (b) Upper left: High-resolution HAADF–STEM image taken from the outermost surface of a single SC CoO NR revealing the exposed {111} nanofacets, with inset showing the corresponding selected area electron diffraction pattern taken from [110] zone axis. Scale bar is 2 nm. Experimental and simulated HADDF–STEM images of the pyramidal structure, respectively. Scale bar is 1 nm. Atomic model of a nanopyramid enclosed with {100} and {111} facets, and the projection of this pyramidal structure along [110] zone axis. Bottom left: OER LSVs of SC, PC CoO NRs and commercial RuO_2 catalysts directly deposited on CFP in O_2-saturated 1 M KOH solution at scan rate of 0.5 mV s^{-1} without iR correction, with the corresponding OER Tafel plots shown in inset. Upper right: The calculated ORR/OER free energy diagram at the equilibrium potential on different facets. Bottom right: The projected density of states (PDOS) on pristine CoO and CoO with O-vacancies. Reproduced with permission.[264] Copyright 2016 Springer Nature.

of 220 mV and improved electrical conductivity. In addition, superfluous V_O will affect the stability of electrodes, filling heteroatoms in favor of compensating the coordination numbers and increasing the binding between intermediates and surface of electrocatalysts.[266]

Defects can also cause charge compensation and also play as scattering centers to affect the transport properties like mobility and conductivity, and even create lattice distortions and form strain. Cheng *et al.* prepared a rutile β-MnO_2 with native V_O, and the charge is compensated by the reduction of Mn^{4+} to Mn^{3+}.[267] It is remarkable that a new crystal structure appeared except a typical pyrolusite lattice, which can be explained by introduced V_O. In this case, electrodes exhibit a more positive potential and a large current for ORR. The work of Zhao *et al.* emphasized that the Mn^{3+} active sites of ultrathin δ-MnO_2 nanosheets contribute to half-metallicity and strong H_2O adsorption.[268] There are two valences, Co^{2+} and Co^{3+}, in Co_3O_4. Some studies have demonstrated that Co^{3+} is the key active site of the ORR, and that relative ratio of Co^{2+}/Co^{3+} can be tuned by controlling the concentration of V_O.[266,269] Besides, the methane catalytic combustion of Ca-doped $LaFeO_3$ perovskites show a directly correlation to the amount of Fe^{4+}, which results from the formation of V_O.[270]

In addition, grain boundaries, steps, and edges also belong to defects. It is generally true that these defects are thermodynamically unstable, and have high energy and low coordination number, which leads to improved electrocatalytic performance. The broken symmetry near grain boundaries increases the binding energy of intermediate species.[271,272] However, in some cases of photocatalysis, it is easy to be trapped and recombined when charge carriers transfer through the grain boundaries and then inhibit catalytic activity.[273,274]

3.9 Ionic doping

Ionotronics is an emerging technology that aims to induce a large change of transport properties through the movement of ionic doping by an external stimuli. By moving ions, such as H^+, Li^+, Na^+ and Mg^{2+}, into or out of TMOs under an electric field, reversible changes in the structure, electronic structure and physical properties of TMOs can be achieved. Ionic doping across solid–liquid interfaces can be realized using ionic liquid, aqueous solutions or water. In ionic liquid gating, due to a very strong electric field (≥ 10 MV cm^{-1}) formed at the interface, hydrogen ions can be intercalated into TMOs from the ionic liquid, or oxygen ions can be moved out from TMOs, depending on the polarity of the electric field. As shown in Fig. 11a, using ionic liquids, controlling the insertion and extraction of hydrogen and oxygen ions independently of each other can direct reversible phase transformations among three different materials phases: $HSrCoO_{2.5}$, brownmillerite $SrCoO_{2.5}$ and perovskite $SrCoO_3$.[275] Consequently, Lu *et al.* observed a dramatic modulation of electronic, magnetic and optical properties by changing the valence state of Co and Co 3d and O 2p orbital hybridization. Moreover, the electric-field control of three different magnetic ground states was also reported (Fig. 11b).[19] Very recently, the tuning of thermal conductivity was further demonstrated by triggering the "tri-state" phase transitions in $SrCoO_{2.5}$ films (Fig. 11c).[275] Similar reversible phase transformations mediated by hydrogen and oxygen ions was also observed in VO_2, ZnO, WO_3, $SrRuO_3$, $La_{1-x}Sr_xMnO_3$, $La_{0.7}Sr_{0.3}MnO_3/SrIrO_3$ superlattice films, *etc.*[18,164,276–281] Water was also used as a gating medium for achieving hydrogen doping.[282] The ionization of water to form H^+ and OH^- occurs when a bias voltage over 1.23 V is applied between an electrode and TMOs in water. Thus, under a positive electric field, H^+ can be intercalated into TMOs.
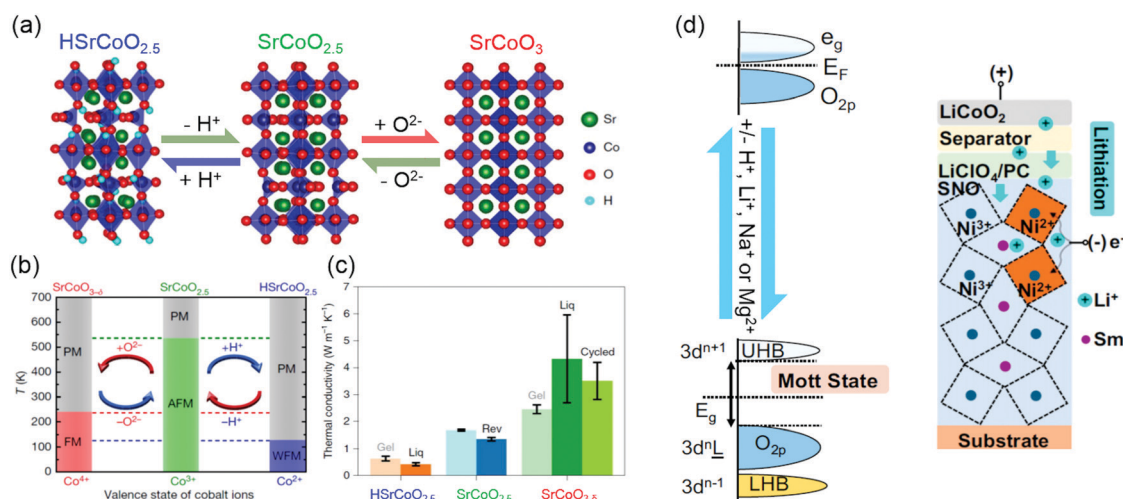
Fig. 11 (a) Reversible phase transformation of $SrCoO_{2.5}$ through the dual-ion (O^{2-} and H^+) switch. Reproduced with permission.[275] Copyright 2020 Springer Nature. (b) Magnetoelectric effects in different temperature regions. Red and blue arrows represent negative and positive voltages, respectively. PM, paramagnetism; FM, ferromagnetism; AFM, antiferromagnetism; WFM, weak ferromagnetism. Reproduced with permission.[19] Copyright 2017 Springer Nature. (c) Thermal conductivities of $HSrCoO_{2.5}$, $SrCoO_{2.5}$ and $SrCoO_{3-\delta}$ films. Reproduced with permission.[275] Copyright 2020 Springer Nature. (d) Left panel: Band diagram of $SmNiO_3$ before (top) and after ionic doping (bottom). E_g is the band gap. Right panel: Electrochemical cell for lithiation of $SmNiO_3$. Reproduced with permission.[286] Copyright 2018 National Academy of Sciences.

It has been reported that a water-infiltrated nanoporous glass or a humid air gap can be used for controlling the channel conductance in $SrTiO_3$ and VO_2 field effect transistors, respectively.[283,284] In addition, H^+ doping through solid–gas interface was studied in $SmNiO_3$ and VO_2 films.[20,276,285] Pt electrodes were used for achieving effective H^+ doping, which changes electron doping and suppresses the electronic transport *via* electron–electron correlations.[20]

Ionic doping across solid–solid interfaces can be realized using solid state electrolytes. When a positive bias is applied across a proton-storing solid-state electrolyte, hydrogen ions can be injected into TMOs. The advantage of this doping method is that not only H^+ but also Li^+, Na^+, and Mg^{2+} intercalation can take place in a controlled manner by gating through electrochemical cells. As shown in Fig. 11d, pristine room temperature $SmNiO_3$ is a semiconductor with a narrow bandgap.[20,286] After ionic doping, it becomes a strongly correlated insulator, with a bandgap on the order of 3 eV, where Ni^{3+} is reduced to Ni^{2+}. Furthermore, electric-field-induced ion injection is non-volatile and reversible. After removal of an applied electric field, ionic dopants remain in TMOs, and the application of a reverse electric-field can be used to remove them. Therefore, these phenomena can be exploited for the use in non-volatile memory devices with cross-bar or related geometries.

The reversible manipulation of physical and chemical properties in TMOs using ionic doping can be used in a wide range of applications, such as electronics (*e.g.*, sensors,[287] non-volatile memory,[288] smart windows, *etc.*),[19,289] energy (*e.g.*, catalysis for water splitting, fuel cell, *etc.*),[290–292] and emerging research directions (*e.g.*, biomimetric machine learning, synaptic transistor, *etc.*).[179,293–296] More comprehensive discussions on these topics can be found in recent published reviews.[21,282,297]

3.10 Wide bandgap oxide semiconductors

Wide bandgap oxide semiconductors are widely utilized in the field of flat-panel displays (FPDs), sensing devices and power electronics due to their fascinating opto-electrical properties, compositional diversities, structural stability and adjustable bandgap values.[43,298–301] Motivated by the great promises of oxide semiconductors and devices, great efforts have been made to modulate their performances from different angles including mobility, carrier type (electron or hole), crystallinity, transparency, *etc.* Defect engineering has been one of the core strategies in controlling oxide semiconductor properties.[302–304] Here we will take some representative oxide semiconductors (ZnO, In_2O_3, IGZO) as examples, to discuss how the control of defects, such as V_O, V_C and interstitials, could help to shape materials and devices.

ZnO is probably the most remarkable oxide semiconductor. With a direct bandgap of 3.4 eV, large exciton energy (60 meV), low cost and easiness of growing large single crystals, ZnO seems like a very attractive candidate for optoelectronics.[305,306] Despite its intrinsic advantages, the lack of control over dopants and defects hindered its further application to practical devices,

thus stimulated a boom over investigating the defect chemistry in ZnO.[302,307–310] The as-grown ZnO crystals normally exhibit n-type conductivity, which was initially attributed to the native defects such as Zn interstitials, Zn vacancies or V_O (Fig. 12a).[302,305] However, V_O has been proven to be deep donors[311–313] and Zn vacancies form as compensating acceptors in n-type ZnO.[314,315] Zn interstitials are proved to be shallow donors,[315,316] yet they are unstable at room temperature due to their mobile nature.[317,318] Group-III donors (B, Al, Ga, and In) and H impurities account for most of the n-type conductivity in ZnO samples. To reach an applicable doping level of $n \sim 10^{20}$ cm^{-3} as required by a transparent conductor, H is a shallow donor in ZnO and has been shown great improvement of carrier concentrations with the magnitude of 3 orders.[319–322] Despite multiple experimental and theoretical investigations having been devoted to the microscopic structure of H in defects[323–326] and its complex with Zn vacancies or other impurities,[327–329] its interaction with the ZnO crystal lattice or components and the mechanism of modulating carrier transportation are still not very clear.

In_2O_3 is firstly known as the parent material of widely used transparent semiconducting oxide indium-tin-oxide (ITO).[330–333] In the last decade, In_2O_3 itself has been rediscovered to be a wide-bandgap semiconductor with great potential and has received lots of attentions from the semiconductor physics community,[299] due to its fascinating structural,[334–337] mechanical[338–340] and electronic properties.[341–344] The explorations of the influence of defects on conductivity of In_2O_3 has a long history. Bierwagen *et al.* summarized the results of Hall mobility and Hall electron concentration in unintentionally doped, In_2O_3 thin films and bulk samples and observed a qualitatively similar trend, that simultaneously increased in electron mobility and decreased electron concentration, consistent with O_2 annealing reduced donor concentration, as shown in Fig. 12b.[299] Discrepancies remain regarding the nature of native defects. DFT calculations within LDA/GGA by Lany *et al.*[313] and Limpijumnong *et al.*[345] reached the conclusion that V_O are deep donors, while Ágoston *et al.* calculated them to be shallow donors using the hybrid-functional method within DFT.[346,347] Calculations by Tang *et al.* suggested that even though V_O creates deep donor levels,[348] In interstitials lead to shallow donors and their coupling with V_O could give rise to even shallower donors. The native defects also have important influences on the doping modulation of In_2O_3. While dopant solubility is sufficient in In_2O_3, native defects normally act as compensating centers, *i.e.*, donor-type defects V_O and In interstitials tend to counteract p-type doping, while acceptor-type defects, *i.e.* In vacancies and O interstitials, counteract n-type doping.[313,349] The control over the In_2O_3 native defects concentrations could be realized by simply adjusting the growth conditions. For example, V_O could be controlled by varying the growth atmosphere or by adding an additional O_2 annealing process.[350,351]

Amorphous indium gallium zinc oxide (a-IGZO) is one of the most successful commercialized oxide semiconductors in this century, widely used in thin-film transistors (TFTs) for high-resolution displays.[298,352–355] Defects have a significant

Fig. 12 (a) Structural diagram hydrogen defects in ZnO: Interstitial hydrogen donors (bottom) with antibonding (bottom left) and bond-centered (bottom right) configurations, and nitrogen–hydrogen complex (top). The dashed lines indicate broken Zn–O bonds. Reproduced with permission.[302,328] Copyright 2009 American Institue of Phyiscs and Copyright 2007 American Physcial Society. (b) Hall mobility and Hall electron concentration in unintentionally doped (UID), In_2O_3 thin films and bulk samples. The decreasing electron concentration with simultaneous increase of mobility after annealing in oxygen-containing atmosphere is shown. Reproduced with permission.[299] Copyright 2010 American Institue of Phyiscs. (c) Local coordination structures of some oxygen deficiencies in IGZO. The red spheres represent O ions, green spheres are Ga, grey spheres are Zn and pink spheres are In atoms. The red spheres indicated by the arrows are oxygen vacancy sites. 'Corner-shared', 'Free-space' and 'Edge/Face-shared' notation describes the structures around these oxygen vacancy sites. Reproduced with permission.[298] Copyright 2010 Institue of Phyiscs. (d) Summary of known electronic structure of a-IGZO with subgap defects. Reproduced with permission.[304] Copyright 2019 Wiley-VCH.

influence on a-IGZO materials and TFTs, *i.e.*, while most defects are detrimental to device performance, some defects actually play a positive role in improving carrier density.[304,356,357] V_O, metal–metal bonds and H incorporation are the three main defect types present in channel region of a-IGZO TFTs.[358] V_O could participate in several different local coordination structures: (i) 'Corner-share' structure formed by V_O coordinated with small numbers of cations, (ii) 'Free space' structure formed by V_O adjacent to a large open space and (iii) 'Edge/Face-sharing' structure formed by V_O surrounded by many cations, as shown in Fig. 12c.[298] The 'Corner-share' and 'Free space' structures act as both deep and shallow traps, reducing the electron concentration.[359] The deep traps mainly result in the increase of subthreshold swing and indirectly increase the device operating voltage, while shallow traps contribute to the hysteresis in device performance.[360–362] The 'Edge/Face-sharing' structure act as shallow donors, which is the main source of carriers in a-IGZO and thus vital for device charge transport.[298,352,363,364] Several methods have been proposed to control V_O in a-IGZO, including modulating the growth atmosphere (oxygen partial

pressure)[365–367] and post deposition annealing.[368,369] The metal–metal bonds are associated to V_O, formed by the binding of uncoordinated metal ions caused by deficient oxygen to eliminate the dangling bonds.[355] Additional sub-gap states are induced near CBM by metal–metal bonds and could significantly increase the off-state leakage current I_{off}.[356,370,371] Reduction of metal–metal bonds generally follows the path with the decrease of V_O, yet they are harder to eliminate for the additional energy required to break the bonds.[357] The incorporation of hydrogen could happen during annealing processes or by diffusion of other materials in TFT devices, *i.e.*, gate dielectrics, passivation layers or buffer layers.[372–374] The role of hydrogen in a-IGZO varies under different H concentrations. At lower concentrations lower than $\sim 2 \times 10^{21}$ cm^{-3}, hydrogen improves the device performance by passivating O-related defects either through bonding with weakly bound oxygen to form –OH or replacing the V_O, thus reducing hysteresis and increasing carrier density.[375–377] At higher concentrations above 2×10^{21} cm^{-3}, additional hydrogen in a-IGZO might create a conductive channel near the dielectric interface that negatively shifts the

turn-on voltage.[375] Currently reported sub-gap defects and their influences on electronic structure of IGZO are summarized by Ide *et al.*[304] as shown in Fig. 12d.

4. Summary and perspective

Recent progress in the growth of high-quality TMOs epitaxial thin films, together with exploration of new systems and with the application of different stimuli to tune the structures and defects within them, has led to intriguing new physical phenomena. These phenomena are limited not only to the bulk of the films but also to the heterointerfaces between the different materials. There is huge potential range of new applications stemming from these, influencing every sector of industry from transport to energy to ICT to medicine. In this review, we highlight some of the many fascinating physical properties, ranging from insulating to semiconducting or metallic, exhibiting phenomena from ferroelectricity to transparency. We show how the underlying physics relies on the control of electronic structure, which is determined by the partially occupied TM d orbitals, the hybridization between TM d and oxygen 2p orbitals and the corresponding local atomic structures. We also highlight the importance of defects to electronic structure and chemical structure, and show the benefits of precise defect engineering for enhancing physical properties. However, we also show how that the strong influence of defects in TMOs is something of a double-edged sword: certain defects being engineerable and critical for realizing a desired functionality, while others are detrimental to expected properties and hard to control. In this latter regard, there are still many challenges to be solved, some key ones being summarized as following:

(1) Unlike misfit dislocations, grain boundaries and domain walls, point defects formed by cation/oxygen vacancies and ionic doping (*e.g.*, H^+ and Li^+) are 'invisible' because of their dilute concentrations. There is a huge demand for new techniques to be available that can allow us to observe cation/oxygen vacancies and ions at low concentrations and with large spatial accuracy. Therefore, new ways to directly, rapidly and simply characterise these point defects and to quantify their presence are of utmost importance for understanding defect-structure–property relations in memristors, in wide bandgap oxide semiconductors, at functional heterointerfaces, *etc.* With such techniques, a new world will be opened up for TMOs science and applications.

(2) Defects, strain and interfaces are usually entangled for tuning the functionalities in TMOs thin films. Hence, great care must be taken to separate these parameters from one another so as to enable their individual influence on the physical properties to be understood. On the other hand, similar to the implementation of semiconductors in devices, an important question is how to achieve precise control of defect (or impurity) concentrations and distributions in TMOs thin films. This will be important as there is an increasing drive towards miniaturization of electronic circuits and devices

based on TMOs thin films. Furthermore, to achieve novel functionalities which utilise defects, an important question is how to dynamically characterise/control/tune the distribution of defects. To fulfill these purposes, many characterisation techniques (*e.g.*, photoemission spectroscopy, transmission electron microscopy, scanning tunneling microscopy, scanning probe microscopy, X-ray techniques) usually working under vacuum conditions and/or room temperature, need to be customized to work in controlled environments and high temperatures, thereby enabling characterisation under *in situ* or even *in operando* conditions to monitor the dynamics of defects. Also, combining *in situ* and *in operando* techniques and first-principles calculations will allow for increasingly accurate characterisation of defects, strain and interfaces, and undoubtedly will improve the understanding of their individual roles in TMO devices during operation. Further developments in synthesis/growth of TMOs thin films will allow greater control of dynamic ionic defect profiles. In turn, it may be possible to exploit the different mobilities of cations and anions to engineer gradients in static and dynamic chemistry and carrier concentrations.

(3) Electrochemical reactions and ionic transport underpin the functionality of memristors, wide bandgap oxide semiconductors and electrochemical water splitting. When the bias voltage is applied for driving ionic motion, the irreversible/reversible redistribution of defects in TMOs thin films may occur. Consequently, the stability of defects in TMOs thin films is a key problem for the irreversible fatigue/degeneration of electronics and catalysts and needs to be addressed. One approach is to investigate static and dynamic ionic behaviour which will help us to understand the interaction between ionic motion and defects. Further progress, in both experimental and theoretical methodology, will be key for exploring and controlling the stability of defects in TMOs thin films for electronics and energy applications.

Conflicts of interest

The authors declare no competing financial interests.

Acknowledgements

References

1 J. L. MacManus-Driscoll, M. P. Wells, C. Yun, J.-W. Lee, C.-B. Eom and D. G. Schlom, *APL Mater.*, 2020, **8**, 040904.
2 S. A. Chambers, *Surf. Sci. Rep.*, 2000, **39**, 105–180.

3 Z. Huang, A. Ariando, X. Renshaw Wang, A. Rusydi, J. Chen, H. Yang and T. Venkatesan, *Adv. Mater.*, 2018, **30**, 1802439.

4 S. Saremi, R. Gao, A. Dasgupta and L. W. Martin, *Am. Ceram. Soc. Bull.*, 2018, **97**, 16–23.

5 J. F. Schooley, W. R. Hosler and M. L. Cohen, *Phys. Rev. Lett.*, 1964, **12**, 474–475.

6 J. F. Schooley, W. R. Hosler, E. Ambler, J. H. Becker, M. L. Cohen and C. S. Koonce, *Phys. Rev. Lett.*, 1965, **14**, 305–307.

7 C. S. Koonce, M. L. Cohen, J. F. Schooley, W. R. Hosler and E. R. Pfeiffer, *Phys. Rev.*, 1967, **163**, 380–390.

8 W. D. Rice, P. Ambwani, M. Bombeck, J. D. Thompson, G. Haugstad, C. Leighton and S. A. Crooker, *Nat. Mater.*, 2014, **13**, 481–487.

9 D. Lee, H. Lu, Y. Gu, S.-Y. Choi, S.-D. Li, S. Ryu, T. R. Paudel, K. Song, E. Mikheev, S. Lee, S. Stemmer, D. A. Tenne, S. H. Oh, E. Y. Tsymbal, X. Wu, L.-Q. Chen, A. Gruverman and C. B. Eom, *Science*, 2015, **349**, 1314–1317.

10 K. Klyukin and V. Alexandrov, *Phys. Rev. B*, 2017, **95**, 035301.

11 I. Sugiyama, N. Shibata, Z. Wang, S. Kobayashi, T. Yamamoto and Y. Ikuhara, *Nat. Nanotechnol.*, 2013, **8**, 266–270.

12 R. Gross, L. Alff, B. Büchner, B. H. Freitag, C. Höfener, J. Klein, Y. Lu, W. Mader, J. B. Philipp, M. S. R. Rao, P. Reutler, S. Ritter, S. Thienhaus, S. Uhlenbruck and B. Wiedenhorst, *J. Magn. Magn. Mater.*, 2000, **211**, 150–159.

13 Z. Zhang, W. Sigle and M. Rühle, *Phys. Rev. B: Condens. Matter Mater. Phys.*, 2002, **66**, 094108.

14 P. Gao, S. Yang, R. Ishikawa, N. Li, B. Feng, A. Kumamoto, N. Shibata, P. Yu and Y. Ikuhara, *Phys. Rev. Lett.*, 2018, **120**, 267601.

15 J. Seidel, L. W. Martin, Q. He, Q. Zhan, Y. H. Chu, A. Rother, M. E. Hawkridge, P. Maksymovych, P. Yu, M. Gajek, N. Balke, S. V. Kalinin, S. Gemming, F. Wang, G. Catalan, J. F. Scott, N. A. Spaldin, J. Orenstein and R. Ramesh, *Nat. Mater.*, 2009, **8**, 229–234.

16 M. L. Medarde, *J. Phys.: Condens. Matter*, 1997, **9**, 1679–1707.

17 H. Y. Hwang, S. W. Cheong, P. G. Radaelli, M. Marezio and B. Batlogg, *Phys. Rev. Lett.*, 1995, **75**, 914–917.

18 H. Yuan, H. Shimotani, A. Tsukazaki, A. Ohtomo, M. Kawasaki and Y. Iwasa, *J. Am. Chem. Soc.*, 2010, **132**, 6672–6678.

19 N. Lu, P. Zhang, Q. Zhang, R. Qiao, Q. He, H.-B. Li, Y. Wang, J. Guo, D. Zhang, Z. Duan, Z. Li, M. Wang, S. Yang, M. Yan, E. Arenholz, S. Zhou, W. Yang, L. Gu, C.-W. Nan, J. Wu, Y. Tokura and P. Yu, *Nature*, 2017, **546**, 124–128.

20 J. Shi, Y. Zhou and S. Ramanathan, *Nat. Commun.*, 2014, **5**, 4860.

21 H.-T. Zhang, Z. Zhang, H. Zhou, H. Tanaka, D. D. Fong and S. Ramanathan, *Adv. Phys.: X*, 2019, **4**, 1523686.

22 J. B. Goodenough, *Rep. Prog. Phys.*, 2004, **67**, 1915–1993.

23 H. L. Tuller and S. R. Bishop, *Annu. Rev. Mater. Res.*, 2011, **41**, 369–398.

24 S. V. Kalinin and N. A. Spaldin, *Science*, 2013, **341**, 858–859.

25 A. Herklotz, D. Lee, E.-J. Guo, T. L. Meyer, J. R. Petrie and H. N. Lee, *J. Phys.: Condens. Matter*, 2017, **29**, 493001.

26 A. De Vita, M. J. Gillan, J. S. Lin, M. C. Payne, I. Štich and L. J. Clarke, *Phys. Rev. B: Condens. Matter Mater. Phys.*, 1992, **46**, 12964–12973.

27 A. Gibson, R. Haydock and J. P. LaFemina, *Phys. Rev. B: Condens. Matter Mater. Phys.*, 1994, **50**, 2582–2592.

28 M. V. Ganduglia-Pirovano, A. Hofmann and J. Sauer, *Surf. Sci. Rep.*, 2007, **62**, 219–270.

29 K. H. L. Zhang, G. Li, S. R. Spurgeon, L. Wang, P. Yan, Z. Wang, M. Gu, T. Varga, M. E. Bowden, Z. Zhu, C. Wang and Y. Du, *ACS Appl. Mater. Interfaces*, 2018, **10**, 17480–17486.

30 J. Robertson, *J. Appl. Phys.*, 2003, **93**, 1054–1059.

31 F. El-Mellouhi, E. N. Brothers, M. J. Lucero and G. E. Scuseria, *J. Phys.: Condens. Matter*, 2013, **25**, 135501.

32 T. Shi, Y. Chen and X. Guo, *Prog. Mater. Sci.*, 2016, **80**, 77–132.

33 S. Lany, J. Osorio-Guillén and A. Zunger, *Phys. Rev. B: Condens. Matter Mater. Phys.*, 2007, **75**, 241203.

34 W.-L. Jang, Y.-M. Lu, W.-S. Hwang, T.-L. Hsiung and H. P. Wang, *Appl. Phys. Lett.*, 2009, **94**, 062103.

35 X. Huang, J. Zhang, M. Wu, S. Zhang, H. Xiao, W. Han, T.-L. Lee, A. Tadich, D.-C. Qi, L. Qiao, L. Chen and K. H. L. Zhang, *Phys. Rev. B*, 2019, **100**, 115301.

36 H. Raebiger, S. Lany and A. Zunger, *Phys. Rev. B: Condens. Matter Mater. Phys.*, 2007, **76**, 045209.

37 J. Y. Zhang, W. W. Li, R. L. Z. Hoye, J. L. MacManus-Driscoll, M. Budde, O. Bierwagen, L. Wang, Y. Du, M. J. Wahila, L. F. J. Piper, T. L. Lee, H. J. Edwards, V. R. Dhanak and K. H. L. Zhang, *J. Mater. Chem. C*, 2018, **6**, 2275–2282.

38 S.-H. Yoon and H. Kim, *J. Appl. Phys.*, 2002, **92**, 1039–1047.

39 P. Blennow, A. Hagen, K. K. Hansen, L. R. Wallenberg and M. Mogensen, *Solid State Ionics*, 2008, **179**, 2047–2058.

40 T. Saitoh, A. E. Bocquet, T. Mizokawa, H. Namatame, A. Fujimori, M. Abbate, Y. Takeda and M. Takano, *Phys. Rev. B: Condens. Matter Mater. Phys.*, 1995, **51**, 13942–13951.

41 K. Horiba, A. Chikamatsu, H. Kumigashira, M. Oshima, N. Nakagawa, M. Lippmaa, K. Ono, M. Kawasaki and H. Koinuma, *Phys. Rev. B: Condens. Matter Mater. Phys.*, 2005, **71**, 155420.

42 K. H. L. Zhang, Y. Du, A. Papadogianni, O. Bierwagen, S. Sallis, L. F. Piper, M. E. Bowden, V. Shutthanandan, P. V. Sushko and S. A. Chambers, *Adv. Mater.*, 2015, **27**, 5191–5195.

43 K. H. L. Zhang, K. Xi, M. G. Blamire and R. G. Egdell, *J. Phys.: Condens. Matter*, 2016, **28**, 383002.

44 M. Dawber, K. M. Rabe and J. F. Scott, *Rev. Mod. Phys.*, 2005, **77**, 1083–1130.

45 N. Setter, D. Damjanovic, L. Eng, G. Fox, S. Gevorgian, S. Hong, A. Kingon, H. Kohlstedt, N. Y. Park, G. B. Stephenson, I. Stolitchnov, A. K. Taganstev, D. V. Taylor, T. Yamada and S. Streiffer, *J. Appl. Phys.*, 2006, **100**, 051606.

46 G. H. Haertling, *J. Am. Ceram. Soc.*, 1999, **82**, 797–818.

47 J. F. Scott, *Science*, 2007, **315**, 954–959.

48 A. Kursumovic, W. W. Li, S. Cho, P. J. Curran, D. H. L. Tjhe and J. L. MacManus-Driscoll, *Nano Energy*, 2020, **71**, 104536.

49 R. Mishra, Y.-M. Kim, J. Salafranca, S. K. Kim, S. H. Chang, A. Bhattacharya, D. D. Fong, S. J. Pennycook, S. T. Pantelides and A. Y. Borisevich, *Nano Lett.*, 2014, **14**, 2694–2701.

50 O. Chmaissem, B. Dabrowski, S. Kolesnik, J. Mais, D. E. Brown, R. Kruk, P. Prior, B. Pyles and J. D. Jorgensen, *Phys. Rev. B: Condens. Matter Mater. Phys.*, 2001, **64**, 134412.

51 C. Becher, L. Maurel, U. Aschauer, M. Lilienblum, C. Magén, D. Meier, E. Langenberg, M. Trassin, J. Blasco, I. P. Krug, P. A. Algarabel, N. A. Spaldin, J. A. Pardo and M. Fiebig, *Nat. Nanotechnol.*, 2015, **10**, 661–665.

52 H. Kim, J. Y. Zhang, S. Raghavan and S. Stemmer, *Phys. Rev. X*, 2016, **6**, 041063.

53 D. Lee, B. C. Jeon, S. H. Baek, S. M. Yang, Y. J. Shin, T. H. Kim, Y. S. Kim, J.-G. Yoon, C. B. Eom and T. W. Noh, *Adv. Mater.*, 2012, **24**, 6490–6495.

54 A. R. Damodaran, E. Breckenfeld, Z. Chen, S. Lee and L. W. Martin, *Adv. Mater.*, 2014, **26**, 6341–6347.

55 X. Ren, *Nat. Mater.*, 2004, **3**, 91–94.

56 S. Saremi, J. Kim, A. Ghosh, D. Meyers and L. W. Martin, *Phys. Rev. Lett.*, 2019, **123**, 207602.

57 H. Lu, D. Lee, K. Klyukin, L. Tao, B. Wang, H. Lee, J. Lee, T. R. Paudel, L.-Q. Chen, E. Y. Tsymbal, V. Alexandrov, C.-B. Eom and A. Gruverman, *Nano Lett.*, 2018, **18**, 491–497.

58 R. Gao, S. E. Reyes-Lillo, R. Xu, A. Dasgupta, Y. Dong, L. R. Dedon, J. Kim, S. Saremi, Z. Chen, C. R. Serrao, H. Zhou, J. B. Neaton and L. W. Martin, *Chem. Mater.*, 2017, **29**, 6544–6551.

59 M.-W. Chu, I. Szafraniak, R. Scholz, C. Harnagea, D. Hesse, M. Alexe and U. Gösele, *Nat. Mater.*, 2004, **3**, 87–90.

60 P. Gao, C. T. Nelson, J. R. Jokisaari, S.-H. Baek, C. W. Bark, Y. Zhang, E. Wang, D. G. Schlom, C.-B. Eom and X. Pan, *Nat. Commun.*, 2011, **2**, 591.

61 X. Y. Zhang, R. X. Xu, X. Y. Gao, M. Li, X. N. Shi, Y. D. Ji, F. J. Qian, J. Y. Fan, H. Y. Wang, W.-W. Li and H. Yang, *Appl. Surf. Sci.*, 2020, **516**, 146093.

62 X. Zhang, R. Xu, X. Gao, Y. Ji, F. Qian, J. Fan, H. Wang, W.-W. Li and H. Yang, *J. Mater. Chem. C*, 2020, **8**, 8091.

63 V. Nagarajan, C. L. Jia, H. Kohlstedt, R. Waser, I. B. Misirlioglu, S. P. Alpay and R. Ramesh, *Appl. Phys. Lett.*, 2005, **86**, 192910.

64 A. L. Roytburd, *Phase Transitions*, 1993, **45**, 1–34.

65 J. Seidel, P. Maksymovych, Y. Batra, A. Katan, S. Y. Yang, Q. He, A. P. Baddorf, S. V. Kalinin, C. H. Yang, J. C. Yang, Y. H. Chu, E. K. H. Salje, H. Wormeester, M. Salmeron and R. Ramesh, *Phys. Rev. Lett.*, 2010, **105**, 197603.

66 J. Guyonnet, I. Gaponenko, S. Gariglio and P. Paruch, *Adv. Mater.*, 2011, **23**, 5377–5382.

67 S. Farokhipoor and B. Noheda, *Phys. Rev. Lett.*, 2011, **107**, 127601.

68 S. Y. Yang, J. Seidel, S. J. Byrnes, P. Shafer, C. H. Yang, M. D. Rossell, P. Yu, Y. H. Chu, J. F. Scott, J. W. Ager, L. W. Martin and R. Ramesh, *Nat. Nanotechnol.*, 2010, **5**, 143–147.

69 A. Gupta, G. Q. Gong, G. Xiao, P. R. Duncombe, P. Lecoeur, P. Trouilloud, Y. Y. Wang, V. P. Dravid and J. Z. Sun, *Phys. Rev. B: Condens. Matter Mater. Phys.*, 1996, **54**, R15629–R15632.

70 N. D. Mathur, G. Burnell, S. P. Isaac, T. J. Jackson, B. S. Teo, J. L. MacManus-Driscoll, L. F. Cohen, J. E. Evetts and M. G. Blamire, *Nature*, 1997, **387**, 266–268.

71 U. Aschauer, R. Pfenninger, S. M. Selbach, T. Grande and N. A. Spaldin, *Phys. Rev. B: Condens. Matter Mater. Phys.*, 2013, **88**, 054111.

72 M. Li, C. Tang, T. R. Paudel, D. Song, W. Lü, K. Han, Z. Huang, S. Zeng, X. Renshaw Wang, P. Yang, A. Ariando, J. Chen, T. Venkatesan, E. Y. Tsymbal, C. Li and S. J. Pennycook, *Adv. Mater.*, 2019, **31**, 1901386.

73 S. Cheng, M. Li, S. Deng, S. Bao, P. Tang, W. Duan, J. Ma, C. Nan and J. Zhu, *Adv. Funct. Mater.*, 2016, **26**, 3589–3598.

74 C. G. Shull, W. A. Strauser and E. O. Wollan, *Phys. Rev.*, 1951, **83**, 333–345.

75 K. H. L. Zhang, R. Wu, F. Tang, W. Li, F. E. Oropeza, L. Qiao, V. K. Lazarov, Y. Du, D. J. Payne, J. L. Macmanus-Driscoll and M. G. Blamire, *ACS Appl. Mater. Interfaces*, 2017, **9**, 26549–26555.

76 H. Jeen, W. S. Choi, J. W. Freeland, H. Ohta, C. U. Jung and H. N. Lee, *Adv. Mater.*, 2013, **25**, 3651–3656.

77 K. H. L. Zhang, P. V. Sushko, R. Colby, Y. Du, M. E. Bowden and S. A. Chambers, *Nat. Commun.*, 2014, **5**, 4669.

78 L. Cao, O. Petracic, P. Zakalek, A. Weber, U. Rücker, J. Schubert, A. Koutsioubas, S. Mattauch and T. Brückel, *Adv. Mater.*, 2019, **31**, 1806183.

79 H. Jeen, W. S. Choi, M. D. Biegalski, C. M. Folkman, I. C. Tung, D. D. Fong, J. W. Freeland, D. Shin, H. Ohta, M. F. Chisholm and H. N. Lee, *Nat. Mater.*, 2013, **12**, 1057–1063.

80 J. H. Jang, Y.-M. Kim, Q. He, R. Mishra, L. Qiao, M. D. Biegalski, A. R. Lupini, S. T. Pantelides, S. J. Pennycook, S. V. Kalinin and A. Y. Borisevich, *ACS Nano*, 2017, **11**, 6942–6949.

81 A. Khare, D. Shin, T. S. Yoo, M. Kim, T. D. Kang, J. Lee, S. Roh, I.-H. Jung, J. Hwang, S. W. Kim, T. W. Noh, H. Ohta and W. S. Choi, *Adv. Mater.*, 2017, **29**, 1606566.

82 A. Muñoz, C. De La Calle, J. A. Alonso, P. M. Botta, V. Pardo, D. Baldomir and J. Rivas, *Phys. Rev. B: Condens. Matter Mater. Phys.*, 2008, **78**, 054404.

83 J. Gazquez, S. Bose, M. Sharma, M. A. Torija, S. J. Pennycook, C. Leighton and M. Varela, *APL Mater.*, 2013, **1**, 012105.

84 Y.-M. Kim, J. He, M. D. Biegalski, H. Ambaye, V. Lauter, H. M. Christen, S. T. Pantelides, S. J. Pennycook, S. V. Kalinin and A. Y. Borisevich, *Nat. Mater.*, 2012, **11**, 888–894.

85 M. Merz, P. Nagel, C. Pinta, A. Samartsev, H. v. Löhneysen, M. Wissinger, S. Uebe, A. Assmann, D. Fuchs and S. Schuppler, *Phys. Rev. B: Condens. Matter Mater. Phys.*, 2010, **82**, 174416.

86 W. S. Choi, J.-H. Kwon, H. Jeen, J. E. Hamann-Borrero, A. Radi, S. Macke, R. Sutarto, F. He, G. A. Sawatzky, V. Hinkov, M. Kim and H. N. Lee, *Nano Lett.*, 2012, **12**, 4966–4970.

87 N. Biškup, J. Salafranca, V. Mehta, M. P. Oxley, Y. Suzuki, S. J. Pennycook, S. T. Pantelides and M. Varela, *Phys. Rev. Lett.*, 2014, **112**, 087202.

88 V. V. Mehta, N. Biskup, C. Jenkins, E. Arenholz, M. Varela and Y. Suzuki, *Phys. Rev. B: Condens. Matter Mater. Phys.*, 2015, **91**, 144418.

89 M. B. Salamon and M. Jaime, *Rev. Mod. Phys.*, 2001, **73**, 583–628.

90 J. M. Rondinelli and N. A. Spaldin, *Adv. Mater.*, 2011, **23**, 3363–3381.

91 Y. Tokura and N. Nagaosa, *Science*, 2000, **288**, 462–468.

92 D. Pesquera, G. Herranz, A. Barla, E. Pellegrin, F. Bondino, E. Magnano, F. Sánchez and J. Fontcuberta, *Nat. Commun.*, 2012, **3**, 1189.

93 A. Sadoc, B. Mercey, C. Simon, D. Grebille, W. Prellier and M.-B. Lepetit, *Phys. Rev. Lett.*, 2010, **104**, 046804.

94 L. Qiao, J. H. Jang, D. J. Singh, Z. Gai, H. Xiao, A. Mehta, R. K. Vasudevan, A. Tselev, Z. Feng, H. Zhou, S. Li, W. Prellier, X. Zu, Z. Liu, A. Borisevich, A. P. Baddorf and M. D. Biegalski, *Nano Lett.*, 2015, **15**, 4677–4684.

95 W.-W. Li, B. Zhu, Q. He, A. Y. Borisevich, C. Yun, R. Wu, P. Lu, Z. Qi, Q. Wang, A. Chen, H. Wang, S. A. Cavill, K. H. L. Zhang and J. L. MacManus-Driscoll, *Adv. Sci.*, 2020, **7**, 1901606.

96 J. M. Rondinelli, S. J. May and J. W. Freeland, *MRS Bull.*, 2012, **37**, 261–270.

97 E. J. Moon, R. Colby, Q. Wang, E. Karapetrova, C. M. Schlepütz, M. R. Fitzsimmons and S. J. May, *Nat. Commun.*, 2014, **5**, 5710.

98 J. M. Rondinelli and S. Coh, *Phys. Rev. Lett.*, 2011, **106**, 235502.

99 X. Zhai, L. Cheng, Y. Liu, C. M. Schlepütz, S. Dong, H. Li, X. Zhang, S. Chu, L. Zheng, J. Zhang, A. Zhao, H. Hong, A. Bhattacharya, J. N. Eckstein and C. Zeng, *Nat. Commun.*, 2014, **5**, 4283.

100 A. J. Grutter, A. Vailionis, J. A. Borchers, B. J. Kirby, C. L. Flint, C. He, E. Arenholz and Y. Suzuki, *Nano Lett.*, 2016, **16**, 5647–5651.

101 Z. Liao, M. Huijben, Z. Zhong, N. Gauquelin, S. Macke, R. J. Green, S. Van Aert, J. Verbeeck, G. Van Tendeloo, K. Held, G. A. Sawatzky, G. Koster and G. Rijnders, *Nat. Mater.*, 2016, **15**, 425–431.

102 D. Kan, R. Aso, R. Sato, M. Haruta, H. Kurata and Y. Shimakawa, *Nat. Mater.*, 2016, **15**, 432–437.

103 D. G. Schlom, L.-Q. Chen, C.-B. Eom, K. M. Rabe, S. K. Streiffer and J.-M. Triscone, *Annu. Rev. Mater. Res.*, 2007, **37**, 589–626.

104 N. A. Spaldin and M. Fiebig, *Science*, 2005, **309**, 391–392.

105 W. Eerenstein, N. D. Mathur and J. F. Scott, *Nature*, 2006, **442**, 759–765.

106 R. Ramesh and N. A. Spaldin, *Nat. Mater.*, 2007, **6**, 21–29.

107 K. F. Wang, J. M. Liu and Z. F. Ren, *Adv. Phys.*, 2009, **58**, 321–448.

108 N. A. Spaldin, S.-W. Cheong and R. Ramesh, *Phys. Today*, 2010, **63**, 38.

109 N. A. Hill, *J. Phys. Chem. B*, 2000, **104**, 6694–6709.

110 G. A. Smolenskiĭ and I. E. Chupis, *Phys.-Usp.*, 1982, **25**, 475–493.

111 J. Wang, J. B. Neaton, H. Zheng, V. Nagarajan, S. B. Ogale, B. Liu, D. Viehland, V. Vaithyanathan, D. G. Schlom, U. V. Waghmare, N. A. Spaldin, K. M. Rabe, M. Wuttig and R. Ramesh, *Science*, 2003, **299**, 1719–1722.

112 J. Přívratská and V. Janovec, *Ferroelectrics*, 1997, **204**, 321–331.

113 Q. He, C. H. Yeh, J. C. Yang, G. Singh-Bhalla, C. W. Liang, P. W. Chiu, G. Catalan, L. W. Martin, Y. H. Chu, J. F. Scott and R. Ramesh, *Phys. Rev. Lett.*, 2012, **108**, 067203.

114 A. Lubk, M. D. Rossell, J. Seidel, Y. H. Chu, R. Ramesh, M. J. Hÿtch and E. Snoeck, *Nano Lett.*, 2013, **13**, 1410–1415.

115 P. Agrawal, M. Campanini, A. Rappe, S. Liu, V. Grillo, C. Hébert, R. Erni, D. Passerone and M. D. Rossell, *Phys. Rev. Mater.*, 2019, **3**, 034410.

116 K. T. Kang, C. J. Roh, J. Lim, T. Min, J. H. Lee, K. Lee, T. Y. Lee, S. Kang, D. Seol, J. Kim, H. Ohta, A. Khare, S. Park, Y. Kim, S. C. Chae, Y. S. Oh, J. Lee, J. Yu, J. S. Lee and W. S. Choi, *Adv. Mater.*, 2019, **31**, 1808104.

117 W.-W. Li, R. Zhao, L. Wang, R. Tang, Y. Zhu, J. H. Lee, H. Cao, T. Cai, H. Guo, C. Wang, L. Ling, K. Jin, Y. Zhang, H. Wang, Y. Wang, S. Ju and H. Yang, *Sci. Rep.*, 2013, **3**, 2618.

118 W.-W. Li, Q. He, L. Wang, H. Zeng, J. Bowlan, L. Ling, D. A. Yarotski, W. Zhang, R. Zhao, J. Dai, J. Gu, S. Shen, H. Guo, L. Pi, H. Wang, Y. Wang, I. A. Velasco-Davalos, Y. Wu, Z. Hu, B. Chen, R.-W. Li, Y. Sun, K. Jin, Y. Zhang, H.-T. Chen, S. Ju, A. Ruediger, D. Shi, A. Y. Borisevich and H. Yang, *Phys. Rev. B*, 2017, **96**, 115105.

119 H. Das, A. L. Wysocki, Y. Geng, W. Wu and C. J. Fennie, *Nat. Commun.*, 2014, **5**, 2998.

120 J. A. Mundy, C. M. Brooks, M. E. Holtz, J. A. Moyer, H. Das, A. F. Rébola, J. T. Heron, J. D. Clarkson, S. M. Disseler, Z. Liu, A. Farhan, R. Held, R. Hovden, E. Padgett, Q. Mao, H. Paik, R. Misra, L. F. Kourkoutis, E. Arenholz, A. Scholl, J. A. Borchers, W. D. Ratcliff, R. Ramesh, C. J. Fennie, P. Schiffer, D. A. Muller and D. G. Schlom, *Nature*, 2016, **537**, 523–527.

121 M. J. Pitcher, P. Mandal, M. S. Dyer, J. Alaria, P. Borisov, H. Niu, J. B. Claridge and M. J. Rosseinsky, *Science*, 2015, **347**, 420–424.

122 A. Chen, H. Zhou, Z. Bi, Y. Zhu, Z. Luo, A. Bayraktaroglu, J. Phillips, E.-M. Choi, J. L. MacManus-Driscoll, S. J. Pennycook, J. Narayan, Q. Jia, X. Zhang and H. Wang, *Adv. Mater.*, 2013, **25**, 1028–1032.

123 E.-M. Choi, T. Fix, A. Kursumovic, C. J. Kinane, D. Arena, S.-L. Sahonta, Z. Bi, J. Xiong, L. Yan, J.-S. Lee, H. Wang, S. Langridge, Y.-M. Kim, A. Y. Borisevich, I. MacLaren, Q. M. Ramasse, M. G. Blamire, Q. Jia and J. L. MacManus-Driscoll, *Adv. Funct. Mater.*, 2014, **24**, 7478–7487.

124 C. Homes, T. Vogt, S. Shapiro, S. Wakimoto and A. Ramirez, *Science*, 2001, **293**, 673–676.

125 S. Krohns, P. Lunkenheimer, S. Meissner, A. Reller, B. Gleich, A. Rathgeber, T. Gaugler, H. U. Buhl, D. C. Sinclair and A. Loidl, *Nat. Mater.*, 2011, **10**, 899–901.

126 C.-H. Lee, N. D. Orloff, T. Birol, Y. Zhu, V. Goian, E. Rocas, R. Haislmaier, E. Vlahos, J. A. Mundy, L. F. Kourkoutis, Y. Nie, M. D. Biegalski, J. Zhang, M. Bernhagen, N. A. Benedek, Y. Kim, J. D. Brock, R. Uecker, X. X. Xi, V. Gopalan, D. Nuzhnyy, S. Kamba, D. A. Muller, I. Takeuchi, J. C. Booth, C. J. Fennie and D. G. Schlom, *Nature*, 2013, **502**, 532–536.

127 O. Lee, S. A. Harrington, A. Kursumovic, E. Defay, H. Wang, Z. Bi, C.-F. Tsai, L. Yan, Q. Jia and J. L. MacManus-Driscoll, *Nano Lett.*, 2012, **12**, 4311–4317.

128 A. L. Sangle, O. J. Lee, A. Kursumovic, W. Zhang, A. Chen, H. Wang and J. L. MacManus-Driscoll, *Nanoscale*, 2018, **10**, 3460–3468.

129 H. Yang, H. Wang, J. Yoon, Y. Wang, M. Jain, D. M. Feldmann, P. C. Dowden, J. L. MacManus-Driscoll and Q. Jia, *Adv. Mater.*, 2009, **21**, 3794–3798.

130 R. Zhao, W.-W. Li, A. Chen, W. Zhang, J. Yang, Y. Liang, R. Tang, H. Wang and H. Yang, *Appl. Phys. Lett.*, 2014, **105**, 072907.

131 S. A. Harrington, J. Zhai, S. Denev, V. Gopalan, H. Wang, Z. Bi, S. A. T. Redfern, S.-H. Baek, C. W. Bark, C.-B. Eom, Q. Jia, M. E. Vickers and J. L. MacManus-Driscoll, *Nat. Nanotechnol.*, 2011, **6**, 491–495.

132 W.-W. Li, R. Zhao, R. Tang, A. Chen, W. Zhang, X. Lu, H. Wang and H. Yang, *ACS Appl. Mater. Interfaces*, 2014, **6**, 5356–5361.

133 W.-W. Li, W. Zhang, L. Wang, J. Gu, A. Chen, R. Zhao, Y. Liang, H. Guo, R. Tang, C. Wang, K. Jin, H. Wang and H. Yang, *Sci. Rep.*, 2015, **5**, 11335.

134 W.-W. Li, J. Gu, Q. He, K. H. L. Zhang, C. Wang, K. Jin, Y. Wang, M. Acosta, H. Wang, A. Y. Borisevich, J. L. MacManus-Driscoll and H. Yang, *Appl. Phys. Lett.*, 2018, **112**, 182906.

135 A. Ohtomo and H. Y. Hwang, *Nature*, 2004, **427**, 423–426.

136 S. Thiel, G. Hammerl, A. Schmehl, C. W. Schneider and J. Mannhart, *Science*, 2006, **313**, 1942–1945.

137 Y. Chen, N. Pryds, J. E. Kleibeuker, G. Koster, J. Sun, E. Stamate, B. Shen, G. Rijnders and S. Linderoth, *Nano Lett.*, 2011, **11**, 3774–3778.

138 S. A. Chambers, L. Qiao, T. C. Droubay, T. C. Kaspar, B. W. Arey and P. Sushko, *Phys. Rev. Lett.*, 2011, **107**, 206802.

139 N. Reyren, S. Thiel, A. Caviglia, L. F. Kourkoutis, G. Hammerl, C. Richter, C. W. Schneider, T. Kopp, A.-S. Rüetschi and D. Jaccard, *Science*, 2007, **317**, 1196–1199.

140 J. Mannhart and D. Schlom, *Science*, 2010, **327**, 1607–1611.

141 C. Cen, S. Thiel, J. Mannhart and J. Levy, *Science*, 2009, **323**, 1026–1030.

142 A. D. Caviglia, S. Gariglio, C. Cancellieri, B. Sacépé, A. Fête, N. Reyren, M. Gabay, A. F. Morpurgo and J. M. Triscone, *Phys. Rev. Lett.*, 2010, **105**, 236802.

143 L. Qiao, T. C. Droubay, T. C. Kaspar, P. V. Sushko and S. A. Chambers, *Surf. Sci.*, 2011, **605**, 1381–1387.

144 L. Qiao, T. C. Droubay, T. Varga, M. E. Bowden, V. Shutthanandan, Z. Zhu, T. C. Kaspar and S. A. Chambers, *Phys. Rev. B: Condens. Matter Mater. Phys.*, 2011, **83**, 085408.

145 G. Herranz, M. Basletić, M. Bibes, C. Carrétéro, E. Tafra, E. Jacquet, K. Bouzehouane, C. Deranlot, A. Hamzić, J. M. Broto, A. Barthélémy and A. Fert, *Phys. Rev. Lett.*, 2007, **98**, 216803.

146 W. Siemons, G. Koster, H. Yamamoto, W. A. Harrison, G. Lucovsky, T. H. Geballe, D. H. A. Blank and M. R. Beasley, *Phys. Rev. Lett.*, 2007, **98**, 196802.

147 C. Cancellieri, N. Reyren, S. Gariglio, A. D. Caviglia, A. Fête and J. M. Triscone, *Europhys. Lett.*, 2010, **91**, 17004.

148 A. Brinkman, M. Huijben, M. van Zalk, J. Huijben, U. Zeitler, J. C. Maan, W. G. van der Wiel, G. Rijnders, D. H. A. Blank and H. Hilgenkamp, *Nat. Mater.*, 2007, **6**, 493–496.

149 N. Nakagawa, H. Y. Hwang and D. A. Muller, *Nat. Mater.*, 2006, **5**, 204–209.

150 H. Lee, N. Campbell, J. Lee, T. J. Asel, T. R. Paudel, H. Zhou, J. W. Lee, B. Noesges, J. Seo, B. Park, L. J. Brillson, S. H. Oh, E. Y. Tsymbal, M. S. Rzchowski and C. B. Eom, *Nat. Mater.*, 2018, **17**, 231–236.

151 P. Zubko, S. Gariglio, M. Gabay, P. Ghosez and J.-M. Triscone, *Annu. Rev. Condens. Matter Phys.*, 2011, **2**, 141–165.

152 J. Mannhart, D. H. A. Blank, H. Y. Hwang, A. J. Millis and J. M. Triscone, *MRS Bull.*, 2008, **33**, 1027–1034.

153 S. A. Chambers, M. H. Engelhard, V. Shutthanandan, Z. Zhu, T. C. Droubay, L. Qiao, P. V. Sushko, T. Feng, H. D. Lee, T. Gustafsson, E. Garfunkel, A. B. Shah, J. M. Zuo and Q. M. Ramasse, *Surf. Sci. Rep.*, 2010, **65**, 317–352.

154 M. Imada, A. Fujimori and Y. Tokura, *Rev. Mod. Phys.*, 1998, **70**, 1039–1263.

155 M. Uehara, S. Mori, C. H. Chen and S. W. Cheong, *Nature*, 1999, **399**, 560–563.

156 L. Zhang, C. Israel, A. Biswas, R. Greene and A. De Lozanne, *Science*, 2002, **298**, 805–807.

157 E. Dagotto, *Science*, 2005, **309**, 257–262.

158 K. H. L. Zhang, Y. Du, P. V. Sushko, M. E. Bowden, V. Shutthanandan, S. Sallis, L. F. J. Piper and S. A. Chambers, *Phys. Rev. B: Condens. Matter Mater. Phys.*, 2015, **91**, 155129.

159 Z. Yang, C. Ko and S. Ramanathan, *Annu. Rev. Mater. Res.*, 2011, **41**, 337–367.

160 D. M. Newns, J. A. Misewich, C. C. Tsuei, A. Gupta, B. A. Scott and A. Schrott, *Appl. Phys. Lett.*, 1998, **73**, 780–782.

161 F. J. Morin, *Phys. Rev. Lett.*, 1959, **3**, 34–36.

162 Y. Muraoka and Z. Hiroi, *Appl. Phys. Lett.*, 2002, **80**, 583–585.

163 L. L. Fan, S. Chen, Z. L. Luo, Q. H. Liu, Y. F. Wu, L. Song, D. X. Ji, P. Wang, W. S. Chu, C. Gao, C. W. Zou and Z. Y. Wu, *Nano Lett.*, 2014, **14**, 4036–4043.

164 H. Ji, J. Wei and D. Natelson, *Nano Lett.*, 2012, **12**, 2988–2992.

165 Z. Zhang, F. Zuo, C. Wan, A. Dutta, J. Kim, J. Rensberg, R. Nawrodt, H. H. Park, T. J. Larrabee, X. Guan, Y. Zhou,

S. M. Prokes, C. Ronning, V. M. Shalaev, A. Boltasseva, M. A. Kats and S. Ramanathan, *Phys. Rev. Appl.*, 2017, **7**, 034008.

166 Y. Ji, Q. Yang, X. Zhang, R. Xu, W. Liang, R. Zhao, W. Li, X. Ou and H. Yang, *Appl. Phys. Lett.*, 2019, **115**, 201603.

167 J. Jeong, N. Aetukuri, T. Graf, T. D. Schladt, M. G. Samant and S. S. Parkin, *Science*, 2013, **339**, 1402–1405.

168 Y. Zhou and S. Ramanathan, *J. Appl. Phys.*, 2012, **111**, 084508.

169 D. Lee, B. Chung, Y. Shi, G.-Y. Kim, N. Campbell, F. Xue, K. Song, S.-Y. Choi, J. Podkaminer and T. Kim, *Science*, 2018, **362**, 1037–1040.

170 E. Enriquez, A. Chen, Z. Harrell, X. Lü, P. Dowden, N. Koskelo, M. Janoschek, C. Chen and Q. Jia, *Appl. Phys. Lett.*, 2016, **109**, 141906.

171 S. Catalano, M. Gibert, J. Fowlie, J. Íñiguez, J. M. Triscone and J. Kreisel, *Rep. Prog. Phys.*, 2018, **81**, 046501.

172 R. K. Patel, D. Meyers, X. Liu, P. Mandal, M. Kareev, P. Shafer, J.-W. Kim, P. J. Ryan, S. Middey and J. Chakhalian, *APL Mater.*, 2020, **8**, 041113.

173 J. B. Torrance, P. Lacorre, A. I. Nazzal, E. J. Ansaldo and C. Niedermayer, *Phys. Rev. B: Condens. Matter Mater. Phys.*, 1992, **45**, 8209–8212.

174 T. Mizokawa, D. I. Khomskii and G. A. Sawatzky, *Phys. Rev. B: Condens. Matter Mater. Phys.*, 2000, **61**, 11263–11266.

175 H. Raebiger, S. Lany and A. Zunger, *Nature*, 2008, **453**, 763–766.

176 H. Park, A. J. Millis and C. A. Marianetti, *Phys. Rev. Lett.*, 2012, **109**, 156402.

177 V. Bisogni, S. Catalano, R. J. Green, M. Gibert, R. Scherwitzl, Y. Huang, V. N. Strocov, P. Zubko, S. Balandeh, J.-M. Triscone, G. Sawatzky and T. Schmitt, *Nat. Commun.*, 2016, **7**, 13017.

178 I. V. Nikulin, M. A. Novojilov, A. R. Kaul, S. N. Mudretsova and S. V. Kondrashov, *Mater. Res. Bull.*, 2004, **39**, 775–791.

179 J. Shi, S. D. Ha, Y. Zhou, F. Schoofs and S. Ramanathan, *Nat. Commun.*, 2013, **4**, 2676.

180 M. Kawai, S. Inoue, M. Mizumaki, N. Kawamura, N. Ichikawa and Y. Shimakawa, *Appl. Phys. Lett.*, 2009, **94**, 082102.

181 M. Kotiuga, Z. Zhang, J. Li, F. Rodolakis, H. Zhou, R. Sutarto, F. He, Q. Wang, Y. Sun and Y. Wang, *Proc. Natl. Acad. Sci. U. S. A.*, 2019, **116**, 21992–21997.

182 A. Mercy, J. Bieder, J. Íñiguez and P. Ghosez, *Nat. Commun.*, 2017, **8**, 1677.

183 Z. Liao, N. Gauquelin, R. J. Green, K. Müller-Caspary, I. Lobato, L. Li, S. Van Aert, J. Verbeeck, M. Huijben and M. N. Grisolia, *Proc. Natl. Acad. Sci. U. S. A.*, 2018, **115**, 9515–9520.

184 I. Valov, R. Waser, J. R. Jameson and M. N. Kozicki, *Nanotechnology*, 2011, **22**, 289502.

185 R. Waser and M. Aono, *Nat. Mater.*, 2007, **6**, 833–840.

186 Y. Bernard, V. T. Renard, P. Gonon and V. Jousseaume, *Microelectron. Eng.*, 2011, **88**, 814–816.

187 Y. Yang, P. Gao, S. Gaba, T. Chang, X. Pan and W. Lu, *Nat. Commun.*, 2012, **3**, 732.

188 J. J. Yang, J. Borghetti, D. Murphy, D. R. Stewart and R. S. Williams, *Adv. Mater.*, 2009, **21**, 3754–3758.

189 R. Waser, R. Dittmann, G. Staikov and K. Szot, *Adv. Mater.*, 2009, **21**, 2632–2663.

190 D.-H. Kwon, K. M. Kim, J. H. Jang, J. M. Jeon, M. H. Lee, G. H. Kim, X.-S. Li, G.-S. Park, B. Lee, S. Han, M. Kim and C. S. Hwang, *Nat. Nanotechnol.*, 2010, **5**, 148–153.

191 M.-J. Lee, C. B. Lee, D. Lee, S. R. Lee, M. Chang, J. H. Hur, Y.-B. Kim, C.-J. Kim, D. H. Seo, S. Seo, U. I. Chung, I.-K. Yoo and K. Kim, *Nat. Mater.*, 2011, **10**, 625–630.

192 J.-Y. Chen, C.-L. Hsin, C.-W. Huang, C.-H. Chiu, Y.-T. Huang, S.-J. Lin, W.-W. Wu and L.-J. Chen, *Nano Lett.*, 2013, **13**, 3671–3677.

193 D.-j. Seong, M. Jo, D. Lee and H. Hwang, *Electrochem. Solid-State Lett.*, 2007, **10**, H168.

194 K. M. Kim, B. J. Choi, M. H. Lee, G. H. Kim, S. J. Song, J. Y. Seok, J. H. Yoon, S. Han and C. S. Hwang, *Nanotechnology*, 2011, **22**, 254010.

195 T. Fujii, M. Kawasaki, A. Sawa, Y. Kawazoe, H. Akoh and Y. Tokura, *Phys. Rev. B: Condens. Matter Mater. Phys.*, 2007, **75**, 165101.

196 S. Lee, A. Sangle, P. Lu, A. Chen, W. Zhang, J. S. Lee, H. Wang, Q. Jia and J. L. MacManus-Driscoll, *Adv. Mater.*, 2014, **26**, 6284–6289.

197 S. Cho, C. Yun, S. Tappertzhofen, A. Kursumovic, S. Lee, P. Lu, Q. Jia, M. Fan, J. Jian, H. Wang, S. Hofmann and J. L. MacManus-Driscoll, *Nat. Commun.*, 2016, **7**, 12373.

198 G. Di Martino, S. Tappertzhofen, S. Hofmann and J. Baumberg, *Small*, 2016, **12**, 1334–1341.

199 J. S. Lee, S. Lee and T. W. Noh, *Appl. Phys. Rev.*, 2015, **2**, 031303.

200 J. Zhu, T. Zhang, Y. Yang and R. Huang, *Appl. Phys. Rev.*, 2020, **7**, 011312.

201 Y. Zhang, Z. Wang, J. Zhu, Y. Yang, M. Rao, W. Song, Y. Zhuo, X. Zhang, M. Cui, L. Shen, R. Huang and J. J. Yang, *Appl. Phys. Rev.*, 2020, **7**, 011308.

202 M. Zhao, B. Gao, J. Tang, H. Qian and H. Wu, *Appl. Phys. Rev.*, 2020, **7**, 011301.

203 Z. Wang, H. Wu, G. W. Burr, C. S. Hwang, K. L. Wang, Q. Xia and J. J. Yang, *Nat. Rev. Mater.*, 2020, **5**, 173–195.

204 L. Malavasi, C. A. Fisher and M. S. Islam, *Chem. Soc. Rev.*, 2010, **39**, 4370–4387.

205 N. Mahato, A. Banerjee, A. Gupta, S. Omar and K. Balani, *Prog. Mater. Sci.*, 2015, **72**, 141–337.

206 A. Chroneos, B. Yildiz, A. Tarancón, D. Parfitt and J. A. Kilner, *Energy Environ. Sci.*, 2011, **4**, 2774–2789.

207 J. Garcia-Barriocanal, A. Rivera-Calzada, M. Varela, Z. Sefrioui, E. Iborra, C. Leon, S. J. Pennycook and J. Santamaria, *Science*, 2008, **321**, 676–680.

208 T. J. Pennycook, M. J. Beck, K. Varga, M. Varela, S. J. Pennycook and S. T. Pantelides, *Phys. Rev. Lett.*, 2010, **104**, 115901.

209 N. Schichtel, C. Korte, D. Hesse and J. Janek, *Phys. Chem. Chem. Phys.*, 2009, **11**, 3043–3048.

210 M. Sillassen, P. Eklund, N. Pryds, E. Johnson, U. Helmersson and J. Bøttiger, *Adv. Funct. Mater.*, 2010, **20**, 2071–2076.

211 X. Aparicio-Anglès and N. H. De Leeuw, *J. Am. Ceram. Soc.*, 2017, **100**, 3329–3339.

212 C. Korte, A. Peters, J. Janek, D. Hesse and N. Zakharov, *Phys. Chem. Chem. Phys.*, 2008, **10**, 4623–4635.

213 A. Peters, C. Korte, D. Hesse, N. Zakharov and J. Janek, *Solid State Ionics*, 2007, **178**, 67–76.

214 I. Kosacki, C. M. Rouleau, P. F. Becher, J. Bentley and D. H. Lowndes, *Solid State Ionics*, 2005, **176**, 1319–1326.

215 S. Azad, O. A. Marina, C. M. Wang, L. Saraf, V. Shutthanandan, D. E. McCready, A. El-Azab, J. E. Jaffe, M. H. Engelhard and C. H. Peden, *Appl. Phys. Lett.*, 2005, **86**, 131906.

216 S. Lee and J. L. MacManus-Driscoll, *APL Mater.*, 2017, **5**, 042304.

217 A. Chen, Q. Su, H. Han, E. Enriquez and Q. Jia, *Adv. Mater.*, 2019, **31**, 1803241.

218 S. Lee, W. Zhang, F. Khatkhatay, H. Wang, Q. Jia and J. L. MacManus-Driscoll, *Nano Lett.*, 2015, **15**, 7362–7369.

219 S. M. Yang, S. Lee, J. Jian, W. Zhang, P. Lu, Q. Jia, H. Wang, T. Won Noh, S. V. Kalinin and J. L. MacManus-Driscoll, *Nat. Commun.*, 2015, **6**, 8588.

220 R. Gao, A. C. P. Jain, S. Pandya, Y. Dong, Y. Yuan, H. Zhou, L. R. Dedon, V. Thoréton, S. Saremi, R. Xu, A. Luo, T. Chen, V. Gopalan, E. Ertekin, J. Kilner, T. Ishihara, N. H. Perry, D. R. Trinkle and L. W. Martin, *Adv. Mater.*, 2020, **32**, 1905178.

221 S. Chu, Y. Cui and N. Liu, *Nat. Mater.*, 2016, **16**, 16–22.

222 K. Sivula and R. van de Krol, *Nat. Rev. Mater.*, 2016, **1**, 15010.

223 J. Jian, G. Jiang, R. van de Krol, B. Wei and H. Wang, *Nano Energy*, 2018, **51**, 457–480.

224 W.-W. Li, K. Jiang, Z. Li, S. Gong, R. L. Z. Hoye, Z. Hu, Y. Song, C. Tian, J. Kim, K. H. L. Zhang, S. Cho and J. L. MacManus-Driscoll, *Adv. Energy Mater.*, 2018, **8**, 1801972.

225 C. Li, Z. Luo, T. Wang and J. Gong, *Adv. Mater.*, 2018, **30**, e1707502.

226 S. Kment, F. Riboni, S. Pausova, L. Wang, L. Wang, H. Han, Z. Hubicka, J. Krysa, P. Schmuki and R. Zboril, *Chem. Soc. Rev.*, 2017, **46**, 3716–3769.

227 G. Wang, H. Wang, Y. Ling, Y. Tang, X. Yang, R. C. Fitzmorris, C. Wang, J. Z. Zhang and Y. Li, *Nano Lett.*, 2011, **11**, 3026–3033.

228 S. Wang, P. Chen, J. H. Yun, Y. Hu and L. Wang, *Angew. Chem., Int. Ed.*, 2017, **56**, 8500–8504.

229 W.-J. Yin, H. Tang, S.-H. Wei, M. M. Al-Jassim, J. Turner and Y. Yan, *Phys. Rev. B: Condens. Matter Mater. Phys.*, 2010, **82**, 045106.

230 C. W. Lai and S. Sreekantan, *Int. J. Hydrogen Energy*, 2013, **38**, 2156–2166.

231 D. A. Wheeler, G. Wang, Y. Ling, Y. Li and J. Z. Zhang, *Energy Environ. Sci.*, 2012, **5**, 6682–6702.

232 J. H. Kennedy, J. Karl and W. Frese, *J. Electrochem. Soc.*, 1978, **125**, 709–714.

233 W.-J. Yin, S.-H. Wei, M. M. Al-Jassim, J. Turner and Y. Yan, *Phys. Rev. B: Condens. Matter Mater. Phys.*, 2011, **83**, 155102.

234 Y. Lin, Y. Xu, M. T. Mayer, Z. I. Simpson, G. McMahon, S. Zhou and D. Wang, *J. Am. Chem. Soc.*, 2012, **134**, 5508–5511.

235 X. Qi, G. She, M. Wang, L. Mu and W. Shi, *Chem. Commun.*, 2013, **49**, 5742–5744.

236 S. Shen, C. X. Kronawitter, D. A. Wheeler, P. Guo, S. A. Lindley, J. Jiang, J. Z. Zhang, L. Guo and S. S. Mao, *J. Mater. Chem. A*, 2013, **1**, 14498–14506.

237 M. Li, Y. Yang, Y. Ling, W. Qiu, F. Wang, T. Liu, Y. Song, X. Liu, P. Fang, Y. Tong and Y. Li, *Nano Lett.*, 2017, **17**, 2490–2495.

238 M. A. Lukowski and S. Jin, *J. Phys. Chem. C*, 2011, **115**, 12388–12395.

239 C. M. Tian, W.-W. Li, Y. M. Lin, Z. Z. Yang, L. Wang, Y. G. Du, H. Y. Xiao, L. Qiao, J. Y. Zhang, L. Chen, D.-C. Qi, J. L. Macmanus-Driscoll and K. H. L. Zhang, *J. Phys. Chem. C*, 2020, **124**, 12548–12558.

240 Z. Fu, T. Jiang, Z. Liu, D. Wang, L. Wang and T. Xie, *Electrochim. Acta*, 2014, **129**, 358–363.

241 N. T. Hahn and C. B. Mullins, *Chem. Mater.*, 2010, **22**, 6474–6482.

242 H. Liao, Y. Fan, Y. Lin, K. Wang, R. Li, X. Chen, K. H. Zhang and Y. Yang, 2020, arXiv preprint, arXiv:2002.02389.

243 W. L. Yongcai Qiu, W. Chen, W. Chen, G. Zhou, P.-C. Hsu, R. Zhang, Z. Liang, S. Fan, Y. Zhang and Y. Cui, *Sci. Adv.*, 2016, **2**, e1501764.

244 J. B. Min Zhou, Y. Xu, J. Zhang, J. Xie, M. Guan, C. Wang, L. Wen, Y. Lei and Y. Xie, *ACS Nano*, 2014, **8**, 7088–7098.

245 S. P. Berglund, A. J. E. Rettie, S. Hoang and C. B. Mullins, *Phys. Chem. Chem. Phys.*, 2012, **14**, 7065–7075.

246 F. F. Abdi, N. Firet and R. van de Krol, *ChemCatChem*, 2013, **5**, 490–496.

247 B. J. Morgan and G. W. Watson, *Phys. Rev. B: Condens. Matter Mater. Phys.*, 2009, **80**, 233102.

248 A. Janotti, J. B. Varley, P. Rinke, N. Umezawa, G. Kresse and C. G. Van de Walle, *Phys. Rev. B: Condens. Matter Mater. Phys.*, 2010, **81**, 085212.

249 H. Cui, W. Zhao, C. Yang, H. Yin, T. Lin, Y. Shan, Y. Xie, H. Gu and F. Huang, *J. Mater. Chem. A*, 2014, **2**, 8612–8616.

250 Z. Wang, C. Yang, T. Lin, H. Yin, P. Chen, D. Wan, F. Xu, F. Huang, J. Lin, X. Xie and M. Jiang, *Energy Environ. Sci.*, 2013, **6**, 3007–3014.

251 C. M. Yim, C. L. Pang and G. Thornton, *Phys. Rev. Lett.*, 2010, **104**, 036806.

252 P. T. S. Stefan Wendt, E. Lira, G. K. H. Madsen, Z. Li, J. Ø. Hansen, J. Matthiesen, A. Blekinge-Rasmussen, E. Lægsgaard, B. Hammer and F. Besenbacher, *Science*, 2008, **320**, 1755–1759.

253 J. Gan, X. Lu, J. Wu, S. Xie, T. Zhai, M. Yu, Z. Zhang, Y. Mao, S. C. Wang, Y. Shen and Y. Tong, *Sci. Rep.*, 2013, **3**, 1021.

254 H. L. Tan, A. Suyanto, A. T. D. Denko, W. H. Saputera, R. Amal, F. E. Osterloh and Y. H. Ng, *Part. Part. Syst. Charact.*, 2017, **34**, 1600290.

255 J.-M. Wu, Y. Chen, L. Pan, P. Wang, Y. Cui, D. Kong, L. Wang, X. Zhang and J.-J. Zou, *Appl. Catal., B*, 2018, **221**, 187–195.

256 J. Hu, X. Zhao, W. Chen, H. Su and Z. Chen, *J. Phys. Chem. C*, 2017, **121**, 18702–18709.

257 A. Bergmann, E. Martinez-Moreno, D. Teschner, P. Chernev, M. Gliech, J. F. de Araujo, T. Reier, H. Dau and P. Strasser, *Nat. Commun.*, 2015, **6**, 8625.

258 J. T. Mefford, X. Rong, A. M. Abakumov, W. G. Hardin, S. Dai, A. M. Kolpak, K. P. Johnston and K. J. Stevenson, *Nat. Commun.*, 2016, **7**, 11053.

259 X. Rong, J. Parolin and A. M. Kolpak, *ACS Catal.*, 2016, **6**, 1153–1158.

260 T. Zhang, M.-Y. Wu, D.-Y. Yan, J. Mao, H. Liu, W.-B. Hu, X.-W. Du, T. Ling and S.-Z. Qiao, *Nano Energy*, 2018, **43**, 103–109.

261 M. Cui, X. Ding, X. Huang, Z. Shen, T.-L. Lee, F. E. Oropeza, J. P. Hofmann, E. J. M. Hensen and K. H. L. Zhang, *Chem. Mater.*, 2019, **31**, 7618–7625.

262 G. Fu, X. Wen, S. Xi, Z. Chen, W.-W. Li, J.-Y. Zhang, A. Tadich, R. Wu, D.-C. Qi, Y. Du, J. Cheng and K. H. L. Zhang, *Chem. Mater.*, 2019, **31**, 419–428.

263 Z. Shen, Y. Zhuang, W.-W. Li, X. Huang, F. E. Oropeza, E. J. M. Hensen, J. P. Hofmann, M. Cui, A. Tadich, D. Qi, J. Cheng, J. Li and K. H. L. Zhang, *J. Mater. Chem. A*, 2020, **8**, 4407–4415.

264 T. Ling, D. Y. Yan, Y. Jiao, H. Wang, Y. Zheng, X. Zheng, J. Mao, X. W. Du, Z. Hu, M. Jaroniec and S. Z. Qiao, *Nat. Commun.*, 2016, **7**, 12876.

265 Z. Cai, Y. Bi, E. Hu, W. Liu, N. Dwarica, Y. Tian, X. Li, Y. Kuang, Y. Li, X.-Q. Yang, H. Wang and X. Sun, *Adv. Energy Mater.*, 2018, **8**, 1701694.

266 Z. Xiao, Y. Wang, Y.-C. Huang, Z. Wei, C.-L. Dong, J. Ma, S. Shen, Y. Li and S. Wang, *Energy Environ. Sci.*, 2017, **10**, 2563–2569.

267 F. Cheng, T. Zhang, Y. Zhang, J. Du, X. Han and J. Chen, *Angew. Chem., Int. Ed.*, 2013, **52**, 2474–2477.

268 Y. Zhao, C. Chang, F. Teng, Y. Zhao, G. Chen, R. Shi, G. I. N. Waterhouse, W. Huang and T. Zhang, *Adv. Energy Mater.*, 2017, **7**, 1700005.

269 A. Restovic, E. Ríos, S. Barbato, J. Ortiz and J. L. Gautier, *J. Electroanal. Chem.*, 2002, **522**, 141–151.

270 G. Pecchi, M. G. Jiliberto, A. Buljan and E. J. Delgado, *Solid State Ionics*, 2011, **187**, 27–32.

271 K.-S. Kim, W. J. Kim, H.-K. Lim, E. K. Lee and H. Kim, *ACS Catal.*, 2016, **6**, 4443–4448.

272 Y. Heo, S. Choi, J. Bak, H.-S. Kim, H. B. Bae and S.-Y. Chung, *Adv. Energy Mater.*, 2018, **8**, 1802481.

273 S. Biswas, J. Husek, S. Londo and L. R. Baker, *J. Phys. Chem. Lett.*, 2018, **9**, 5047–5054.

274 M. Zhou, X. W. Lou and Y. Xie, *Nano Today*, 2013, **8**, 598–618.

275 Q. Lu, S. Huberman, H. Zhang, Q. Song, J. Wang, G. Vardar, A. Hunt, I. Waluyo, G. Chen and B. Yildiz, *Nat. Mater.*, 2020, **19**, 655–662.

276 J. Wei, H. Ji, W. Guo, A. H. Nevidomskyy and D. Natelson, *Nat. Nanotechnol.*, 2012, **7**, 357–362.

277 M. Wang, S. Shen, J. Ni, N. Lu, Z. Li, H. B. Li, S. Yang, T. Chen, J. Guo, Y. Wang, H. Xiang and P. Yu, *Adv. Mater.*, 2017, **29**, 1703628.

278 S. Chen, H. Zhou, X. Ye, Z. Chen, J. Zhao, S. Das, C. Klewe, L. Zhang, E. Lupi, P. Shafer, E. Arenholz, D. Jin, H. Huang, Y. Lu, X. Li, M. Wu, S. Ke, H. Xu, X. Zeng, C. Huang, L. W. Martin and L. Chen, *Adv. Funct. Mater.*, 2019, **29**, 1907072.

279 D. Yi, Y. Wang, O. M. J. van 't Erve, L. Xu, H. Yuan, M. J. Veit, P. P. Balakrishnan, Y. Choi, A. T. N'Diaye, P. Shafer, E. Arenholz, A. Grutter, H. Xu, P. Yu, B. T. Jonker and Y. Suzuki, *Nat. Commun.*, 2020, **11**, 902.

280 Z. Li, S. Shen, Z. Tian, K. Hwangbo, M. Wang, Y. Wang, F. M. Bartram, L. He, Y. Lyu, Y. Dong, G. Wan, H. Li, N. Lu, J. Zang, H. Zhou, E. Arenholz, Q. He, L. Yang, W. Luo and P. Yu, *Nat. Commun.*, 2020, **11**, 184.

281 A. Molinari, P. M. Leufke, C. Reitz, S. Dasgupta, R. Witte, R. Kruk and H. Hahn, *Nat. Commun.*, 2017, **8**, 15339.

282 T. Kanki and H. Tanaka, *APL Mater.*, 2017, **5**, 042303.

283 T. Sasaki, H. Ueda, T. Kanki and H. Tanaka, *Sci. Rep.*, 2015, **5**, 17080.

284 H. Ohta, Y. Sato, T. Kato, S. Kim, K. Nomura, Y. Ikuhara and H. Hosono, *Nat. Commun.*, 2010, **1**, 118.

285 H. Yoon, M. Choi, T. W. Lim, H. Kwon, K. Ihm, J. K. Kim, S. Y. Choi and J. Son, *Nat. Mater.*, 2016, **15**, 1113–1119.

286 Y. Sun, M. Kotiuga, D. Lim, B. Narayanan, M. Cherukara, Z. Zhang, Y. Dong, R. Kou, C. J. Sun, Q. Lu, I. Waluyo, A. Hunt, H. Tanaka, A. N. Hattori, S. Gamage, Y. Abate, V. G. Pol, H. Zhou, S. Sankaranarayanan, B. Yildiz, K. M. Rabe and S. Ramanathan, *Proc. Natl. Acad. Sci. U. S. A.*, 2018, **115**, 9672–9677.

287 Z. Zhang, D. Schwanz, B. Narayanan, M. Kotiuga, J. A. Dura, M. Cherukara, H. Zhou, J. W. Freeland, J. Li, R. Sutarto, F. He, C. Wu, J. Zhu, Y. Sun, K. Ramadoss, S. S. Nonnenmann, N. Yu, R. Comin, K. M. Rabe, S. Sankaranarayanan and S. Ramanathan, *Nature*, 2018, **553**, 68–72.

288 U. Bauer, L. Yao, A. J. Tan, P. Agrawal, S. Emori, H. L. Tuller, S. van Dijken and G. S. Beach, *Nat. Mater.*, 2015, **14**, 174–181.

289 D. R. Rosseinsky and R. J. Mortimer, *Adv. Mater.*, 2001, **13**, 783–793.

290 Y. Zhou, X. Guan, H. Zhou, K. Ramadoss, S. Adam, H. Liu, S. Lee, J. Shi, M. Tsuchiya, D. D. Fong and S. Ramanathan, *Nature*, 2016, **534**, 231–234.

291 Y. Koyama, T. E. Chin, U. Rhyner, R. K. Holman, S. R. Hall and Y. M. Chiang, *Adv. Funct. Mater.*, 2006, **16**, 492–498.

292 J. M. McFarland, A. G. Bondy, B. G. Cumming and D. A. Butts, *Nat. Commun.*, 2014, **5**, 4605.

293 C. Ge, C. X. Liu, Q. L. Zhou, Q. H. Zhang, J. Y. Du, J. K. Li, C. Wang, L. Gu, G. Z. Yang and K. J. Jin, *Adv. Mater.*, 2019, **31**, e1900379.

294 H. Y. Huang, C. Ge, Q. H. Zhang, C. X. Liu, J. Y. Du, J. K. Li, C. Wang, L. Gu, G. Z. Yang and K. J. Jin, *Adv. Funct. Mater.*, 2019, **29**, 1902702.

295 C. Ge, G. Li, Q.-l. Zhou, J.-y. Du, E.-j. Guo, M. He, C. Wang, G.-z. Yang and K.-j. Jin, *Nano Energy*, 2020, **67**, 104268.

296 F. Zuo, P. Panda, M. Kotiuga, J. Li, M. Kang, C. Mazzoli, H. Zhou, A. Barbour, S. Wilkins, B. Narayanan, M. Cherukara,

Z. Zhang, S. Sankaranarayanan, R. Comin, K. M. Rabe, K. Roy and S. Ramanathan, *Nat. Commun.*, 2017, **8**, 240.

297 H.-T. Zhang, P. Panda, J. Lin, Y. Kalcheim, K. Wang, J. W. Freeland, D. D. Fong, S. Priya, I. K. Schuller, S. K. R. S. Sankaranarayanan, K. Roy and S. Ramanathan, *Appl. Phys. Rev.*, 2020, **7**, 011309.

298 T. Kamiya, K. Nomura and H. Hosono, *Sci. Technol. Adv. Mater.*, 2010, **11**, 044305.

299 O. Bierwagen and J. S. Speck, *Appl. Phys. Lett.*, 2010, **97**, 072103.

300 Z. Wang, P. K. Nayak, J. A. Caraveo-Frescas and H. N. Alshareef, *Adv. Mater.*, 2016, **28**, 3831–3892.

301 J. Zhang, J. Shi, D.-C. Qi, L. Chen and K. H. L. Zhang, *APL Mater.*, 2020, **8**, 020906.

302 M. D. McCluskey and S. J. Jokela, *J. Appl. Phys.*, 2009, **106**, 071101.

303 J. P. Allen, D. O. Scanlon, L. F. J. Piper and G. W. Watson, *J. Mater. Chem. C*, 2013, **1**, 8194–8208.

304 K. Ide, K. Nomura, H. Hosono and T. Kamiya, *Phys. Status Solidi A*, 2019, **216**, 1800372.

305 Ü. Özgür, Y. I. Alivov, C. Liu, A. Teke, M. Reshchikov, S. Doğan, V. Avrutin, S.-J. Cho and H. Morkoç, *J. Appl. Phys.*, 2005, **98**, 11.

306 S. Liang, H. Sheng, Y. Liu, Z. Huo, Y. Lu and H. Shen, *J. Cryst. Grow.*, 2001, **225**, 110–113.

307 A. Boonchun and W. R. L. Lambrecht, *Phys. Status Solidi B*, 2013, **250**, 2091–2101.

308 F. Xiu, J. Xu, P. C. Joshi, C. A. Bridges and M. Parans Paranthaman, in *Semiconductor Materials for Solar Photovoltaic Cells*, ed. M. P. Paranthaman, W. Wong-Ng and R. N. Bhattacharya, Springer International Publishing, Cham, 2016, DOI: 10.1007/978-3-319-20331-7_4, pp. 105–140.

309 P. Mondal, *Opt. Mater.*, 2019, **98**, 109476.

310 E. Guziewicz, T. A. Krajewski, E. Przezdziecka, K. P. Korona, N. Czechowski, L. Klopotowski and P. Terziyska, *Phys. Status Solidi B*, 2020, **257**, 1900472.

311 A. F. Kohan, G. Ceder, D. Morgan and C. G. Van de Walle, *Phys. Rev. B: Condens. Matter Mater. Phys.*, 2000, **61**, 15019–15027.

312 J. Carrasco, N. Lopez and F. Illas, *Phys. Rev. Lett.*, 2004, **93**, 225502.

313 S. Lany and A. Zunger, *Phys. Rev. Lett.*, 2007, **98**, 045501.

314 F. Tuomisto, V. Ranki, K. Saarinen and D. C. Look, *Phys. Rev. Lett.*, 2003, **91**, 205502.

315 A. Janotti and C. G. Van de Walle, *Phys. Rev. B: Condens. Matter Mater. Phys.*, 2007, **76**, 165202.

316 W. E. Carlos, E. R. Glaser and D. C. Look, *Phys. B*, 2001, **308-310**, 976–979.

317 L. S. Vlasenko and G. D. Watkins, *Phys. Rev. B: Condens. Matter Mater. Phys.*, 2005, **72**, 035203.

318 P. Erhart and K. Albe, *Appl. Phys. Lett.*, 2006, **88**, 201918.

319 C. G. Van de Walle, *Phys. Rev. Lett.*, 2000, **85**, 1012–1015.

320 D. M. Hofmann, A. Hofstaetter, F. Leiter, H. Zhou, F. Henecker, B. K. Meyer, S. B. Orlinskii, J. Schmidt and P. G. Baranov, *Phys. Rev. Lett.*, 2002, **88**, 045504.

321 B. Theys, V. Sallet, F. Jomard, A. Lusson, J.-F. Rommeluère and Z. Teukam, *J. Appl. Phys.*, 2002, **91**, 3922–3924.

322 Y. J. Li, T. C. Kaspar, T. C. Droubay, A. G. Joly, P. Nachimuthu, Z. Zhu, V. Shutthanandan and S. A. Chambers, *J. Appl. Phys.*, 2008, **104**, 053711.

323 A. Janotti and C. G. Van de Walle, *Nat. Mater.*, 2007, **6**, 44–47.

324 Y. J. Li, T. C. Kaspar, T. C. Droubay, Z. Zhu, V. Shutthanandan, P. Nachimuthu and S. A. Chambers, *Appl. Phys. Lett.*, 2008, **92**, 152105.

325 G. A. Shi, M. Saboktakin, M. Stavola and S. J. Pearton, *Appl. Phys. Lett.*, 2004, **85**, 5601–5603.

326 S. Z. Karazhanov and A. G. Ulyashin, *Phys. Rev. B: Condens. Matter Mater. Phys.*, 2008, **78**, 085213.

327 E. V. Lavrov, J. Weber, F. Börrnert, C. G. Van de Walle and R. Helbig, *Phys. Rev. B: Condens. Matter Mater. Phys.*, 2002, **66**, 165205.

328 S. J. Jokela and M. D. McCluskey, *Phys. Rev. B: Condens. Matter Mater. Phys.*, 2007, **76**, 193201.

329 E. V. Lavrov, J. Weber and F. Börrnert, *Phys. Rev. B: Condens. Matter Mater. Phys.*, 2008, **77**, 155209.

330 H. Kim, C. M. Gilmore, A. Piqué, J. S. Horwitz, H. Mattoussi, H. Murata, Z. H. Kafafi and D. B. Chrisey, *J. Appl. Phys.*, 1999, **86**, 6451–6461.

331 C. G. Granqvist and A. Hultåker, *Thin Solid Films*, 2002, **411**, 1–5.

332 A. Bourlange, D. J. Payne, R. G. Palgrave, H. Zhang, J. S. Foord, R. G. Egdell, R. M. J. Jacobs, T. D. Veal, P. D. C. King and C. F. McConville, *J. Appl. Phys.*, 2009, **106**, 013703.

333 K. H. L. Zhang, D. J. Payne and R. G. Egdell, *Solid State Commun.*, 2012, **152**, 194–198.

334 R. A. Cowley, A. Bourlange, J. L. Hutchison, K. H. L. Zhang, A. M. Korsunsky and R. G. Egdell, *Phys. Rev. B: Condens. Matter Mater. Phys.*, 2010, **82**, 165312.

335 K. H. L. Zhang, A. Walsh, C. R. A. Catlow, V. K. Lazarov and R. G. Egdell, *Nano Lett.*, 2010, **10**, 3740–3746.

336 K. H. L. Zhang, A. Regoutz, R. G. Palgrave, D. J. Payne, R. G. Egdell, A. Walsh, S. P. Collins, D. Wermeille and R. A. Cowley, *Phys. Rev. B: Condens. Matter Mater. Phys.*, 2011, **84**, 233301.

337 K. H. L. Zhang, A. Bourlange, R. G. Egdell, S. P. Collins, R. J. Bean, I. K. Robinson and R. A. Cowley, *ACS Nano*, 2012, **6**, 6717–6729.

338 K. H. L. Zhang, V. K. Lazarov, H. H. C. Lai and R. G. Egdell, *J. Cryst. Grow.*, 2011, **318**, 345–350.

339 K. H. L. Zhang, V. K. Lazarov, T. D. Veal, F. E. Oropeza, C. F. McConville, R. G. Egdell and A. Walsh, *J. Phys.: Condens. Matter*, 2011, **23**, 334211.

340 A. Regoutz, R. G. Egdell, D. Wermeille, R. A. Cowley and K. H. L. Zhang, *Nanoscale*, 2013, **5**, 7445–7451.

341 P. D. C. King, T. D. Veal, F. Fuchs, C. Y. Wang, D. J. Payne, A. Bourlange, H. Zhang, G. R. Bell, V. Cimalla, O. Ambacher, R. G. Egdell, F. Bechstedt and C. F. McConville, *Phys. Rev. B: Condens. Matter Mater. Phys.*, 2009, **79**, 205211.

342 K. H. L. Zhang, D. J. Payne, R. G. Palgrave, V. K. Lazarov, W. Chen, A. T. S. Wee, C. F. McConville, P. D. C. King,

T. D. Veal, G. Panaccione, P. Lacovig and R. G. Egdell, *Chem. Mater.*, 2009, **21**, 4353–4355.

343 K. H. L. Zhang, R. G. Egdell, F. Offi, S. Iacobucci, L. Petaccia, S. Gorovikov and P. D. C. King, *Phys. Rev. Lett.*, 2013, **110**, 056803.

344 D. W. Davies, A. Walsh, J. J. Mudd, C. F. McConville, A. Regoutz, J. M. Kahk, D. J. Payne, V. R. Dhanak, D. Hesp, K. Pussi, T.-L. Lee, R. G. Egdell and K. H. L. Zhang, *J. Phys. Chem. C*, 2019, **123**, 1700–1709.

345 S. Limpijumnong, P. Reunchan, A. Janotti and C. G. Van de Walle, *Phys. Rev. B: Condens. Matter Mater. Phys.*, 2009, **80**, 193202.

346 P. Ágoston, K. Albe, R. M. Nieminen and M. J. Puska, *Phys. Rev. Lett.*, 2009, **103**, 245501.

347 P. Ágoston and K. Albe, *Phys. Rev. B: Condens. Matter Mater. Phys.*, 2010, **81**, 195205.

348 L.-M. Tang, L.-L. Wang, D. Wang, J.-Z. Liu and K.-Q. Chen, *J. Appl. Phys.*, 2010, **107**, 083704.

349 J. Robertson, R. Gillen and S. J. Clark, *Thin Solid Films*, 2012, **520**, 3714–3720.

350 O. Bierwagen and J. S. Speck, *Appl. Phys. Lett.*, 2010, **97**, 072103.

351 J. H. W. De Wit, *J. Solid State Chem.*, 1973, **8**, 142–149.

352 K. Nomura, H. Ohta, A. Takagi, T. Kamiya, M. Hirano and H. Hosono, *Nature*, 2004, **432**, 488–492.

353 T. Kamiya, K. Nomura and H. Hosono, *SID Int. Symp. Dig. Tech. Pap.*, 2013, **44**, 11–13.

354 M. Kimura, *Jpn. J. Appl. Phys.*, 2019, **58**, 090503.

355 J. Troughton and D. Atkinson, *J. Mater. Chem. C*, 2019, **7**, 12388–12414.

356 W. H. Han and K. J. Chang, *Phys. Rev. Appl.*, 2016, **6**, 044011.

357 A. de Jamblinne de Meux, G. Pourtois, J. Genoe and P. Heremans, *Phys. Rev. Appl.*, 2018, **9**, 054039.

358 J. S. Park, W.-J. Maeng, H.-S. Kim and J.-S. Park, *Thin Solid Films*, 2012, **520**, 1679–1693.

359 T. Kamiya, K. Nomura, M. Hirano and H. Hosono, *Phys. Status Solidi C*, 2008, **5**, 3098–3100.

360 J. H. Jeong, H. W. Yang, J.-S. Park, J. K. Jeong, Y.-G. Mo, H. D. Kim, J. Song and C. S. Hwang, *Electrochem. Solid-State Lett.*, 2008, **11**, H157.

361 K. Nomura, T. Kamiya and H. Hosono, *J. Soc. Inf. Disp.*, 2010, **18**, 789–795.

362 A. de Jamblinne de Meux, A. Bhoolokam, G. Pourtois, J. Genoe and P. Heremans, *Phys. Status Solidi A*, 2017, **214**, 1600889.

363 J. Yao, N. Xu, S. Deng, J. Chen, J. She, H. D. Shieh, P. Liu and Y. Huang, *IEEE Trans. Electron Devices*, 2011, **58**, 1121–1126.

364 H.-K. Noh, K. J. Chang, B. Ryu and W.-J. Lee, *Phys. Rev. B: Condens. Matter Mater. Phys.*, 2011, **84**, 115205.

365 A. Suresh, P. Gollakota, P. Wellenius, A. Dhawan and J. F. Muth, *Thin Solid Films*, 2008, **516**, 1326–1329.

366 P. Barquinha, A. Vilà, G. Gonçalves, L. Pereira, R. Martins, J. Morante and E. Fortunato, *Phys. Status Solidi A*, 2008, **205**, 1905–1909.

367 J. Chen, L. Wang and X. Su, *Vacuum*, 2012, **86**, 1313–1317.

368 K. H. Ji, J.-I. Kim, H. Y. Jung, S. Y. Park, R. Choi, U. K. Kim, C. S. Hwang, D. Lee, H. Hwang and J. K. Jeong, *Appl. Phys. Lett.*, 2011, **98**, 103509.

369 T. L. Alford, M. J. Gadre and R. N. P. Vemuri, *JOM*, 2013, **65**, 519–524.

370 W. Körner, D. F. Urban and C. Elsässer, *J. Appl. Phys.*, 2013, **114**, 163704.

371 H.-H. Hsieh, T. Kamiya, K. Nomura, H. Hosono and C.-C. Wu, *Appl. Phys. Lett.*, 2008, **92**, 133503.

372 K. Nomura, T. Kamiya, H. Ohta, M. Hirano and H. Hosono, *Appl. Phys. Lett.*, 2008, **93**, 192107.

373 K. Nomura, T. Kamiya and H. Hosono, *ECS J. Solid State Sci. Technol.*, 2012, **2**, P5–P8.

374 Y. Hanyu, K. Domen, K. Nomura, H. Hiramatsu, H. Kumomi, H. Hosono and T. Kamiya, *Appl. Phys. Lett.*, 2013, **103**, 202114.

375 K.-L. Han, K.-C. Ok, H.-S. Cho, S. Oh and J.-S. Park, *Appl. Phys. Lett.*, 2017, **111**, 063502.

376 H.-K. Noh, J.-S. Park and K. J. Chang, *J. Appl. Phys.*, 2013, **113**, 063712.

377 T. Toda, D. Wang, J. Jiang, M. P. Hung and M. Furuta, *IEEE Trans. Electron Devices*, 2014, **61**, 3762–3767.

378 Z. Liu, C. Li, W. Lü, X. Huang, Z. Huang, S. Zeng, X. Qiu, L. Huang, A. Annadi and J. Chen, *Phys. Rev. X*, 2013, **3**, 021010.

379 W.-W. Li, B. Zhu, R. Zhu, Q. Wang, P. Lu, Y. Sun, C. Cafolla, Z. Qi, A. Chen, P. Gao, H. Wang, Q. He, K. H. L. Zhang and J. L. MacManus-Driscoll, *Adv. Funct. Mater.*, 2020, DOI: 10.1002/adfm.202001984.